AGU PUBLICATIONS

JGR

Journal of Geophysical Research: Oceans

RESEARCH ARTICLE

10.1002/2015JC010961

Key Points:

- A new marine radar near-surface vertical current shear retrieval method is introduced
- The mean ~2 m Ekman flow has a ~1.6% speed factor and ~38.9° deflection angle
- The filtered Stokes drift speed at ~2 m is ~50% of the Ekman flow and at ~8 m it is ~25%

Correspondence to:
B. Lund,
blund@rsmas.miami.edu

Citation:
Lund, B., H. C. Graber, H. Tamura, C. O. Collins, and S. M. Varlamov (2015), A new technique for the retrieval of near-surface vertical current shear from marine X-band radar images, *J. Geophys. Res. Oceans*, *120*, 8466–8486, doi:10.1002/2015JC010961.

Received 5 MAY 2015
Accepted 26 NOV 2015
Accepted article online 7 DEC 2015
Published online 30 DEC 2015

A new technique for the retrieval of near-surface vertical current shear from marine X-band radar images

B. Lund[1,2], H. C. Graber[1,2], H. Tamura[3], C. O. Collins III[4], and S. M. Varlamov[3]

[1]Center for Southeastern Tropical Advanced Remote Sensing, University of Miami, Miami, Florida, USA, [2]Now at Department of Ocean Sciences, Rosenstiel School of Marine and Atmospheric Science, University of Miami, Miami, Florida, USA, [3]Marine Information and Tsunami Division, Port and Airport Research Institute, Yokosuka, Japan, [4]Naval Research Laboratory, Stennis Space Center, Mississippi, USA

Abstract A new method to determine near-surface vertical current shear from noncoherent marine X-band radar (MR) data is introduced. A three-dimensional fast Fourier transform is employed to obtain the wave number-frequency spectrum of a MR image sequence. Near-surface currents are estimated from the Doppler-shifted surface gravity wave signal within the spectrum. They represent a weighted mean of the upper ocean flow. The longer the ocean waves on which the current estimates are based, the greater their effective depth. The novelty lies in the wave number-dependent retrieval method, yielding ~100 independent current estimates at effective depths from ~2 to 8 m per ~12 min measurement period. First, MR near-surface vertical current shear measurements are presented using data collected from R/V *Roger Revelle* during the 2010 Impact of Typhoons on the Ocean in the Pacific experiment in the Philippine Sea. Shipboard acoustic Doppler current profiler (ADCP) and anemometer measurements as well as WAVEWATCH III (WW3) model results are used to demonstrate that results are in accord with physical expectations. The wind and wave-driven Ekman flow is obtained by subtracting ADCP-based background currents from the radar measurements. At ~2 m, it is on average ~1.6% of the wind speed and ~38.9° to the right of the wind. With increasing effective depth, the speed factor decreases and the deflection angle increases. Based on WW3 results, the MR-sensed Stokes drift speed is ~50% of the Ekman flow at ~2 m and ~25% at ~8 m. These findings are consistent with previous observations and Ekman theory.

1. Introduction

Near-surface currents are important for multiple reasons. Many key processes controlling climate change occur at the air-sea interface, where the ocean exchanges heat, mass, and momentum with the atmosphere. The wave and wind-driven near-surface currents affecting these processes are still incompletely understood. Accurate near-surface vertical current shear measurements are likely to shed new light on air-sea momentum fluxes. On ships, knowledge about near-surface currents stands to improve operational safety, e.g., when navigating narrow harbor entrances. It may also prove invaluable during search-and-rescue activities, or when monitoring floating pollutants such as oil slicks. Lastly, an accurate understanding of near-surface currents is vital when predicting storm surges, or assessing the hydrodynamic forces acting on offshore platforms. Despite the importance of near-surface currents, measurements are scarce [*Yoshikawa and Masuda*, 2009]. Traditional in situ measurements are difficult to make, and have significant errors due to surface gravity waves and associated mooring motions [*Beardsley et al.*, 1981; *Richman et al.*, 1987]. Modern acoustic Doppler current profiler (ADCP) measurements get contaminated by bubbles, which tend to be present near the surface, especially when wave breaking occurs [*Beal et al.*, 2008; *Firing et al.*, 2012]. Shipboard ADCPs generally do not measure currents in the upper ~20 m of the ocean, since the first few range cells tend to be biased [*Firing and Hummon*, 2010]. Marine X-band radar (MR) data can be analyzed to yield near-surface current information. Shipboard MR currents have the potential to fill the near-surface gap of data, supplementing ADCP measurements.

MR near-surface current retrieval is based on the surface wave signatures within a sequence of backscatter intensity images. The grazing incidence X-band radar return from the sea surface is less well understood than the backscatter at moderate-to-large incidence angles [e.g., *Plant*, 2003]. However, it is generally accepted to be due to a combination of Bragg scatter from centimeter-scale roughness elements [*Barrick*, 1968; *Wright*, 1968] and so-called sea spikes from wave breaking at multiple scales [*Trizna et al.*, 1991]. The MR imaging mechanisms for surface gravity waves (here $>$21 m wavelength) are shadowing (no radar echoes from areas behind wave crests), hydrodynamic modulation (radar scatterers are roughened by wave-induced converging currents and flattened by diverging ones), and tilt modulation (the waves modulate the local incidence angle, which affects backscatter intensity) [*Alpers et al.*, 1981; *Wetzel*, 1990; *Nieto Borge et al.*, 2004].

A new method to retrieve near-surface vertical current shear from MR backscatter data is introduced. Near-surface current vectors can be determined from the Doppler shift that is observed in the wavefield's phase velocities when a current is present. To retrieve near-surface current shear, we exploit the fact that the currents' effective depth increases with the length of the associated waves, as will be explained in the following section. Existing methods yield only a single current vector that, as *Young et al.* [1985a] argue, is representative of the upper $\sim$6 m of the ocean. The promise of MR near-surface vertical current shear measurements has recently been demonstrated in conference proceedings [*Campana et al.*, 2015; *Lund et al.*, 2015a], but not yet in a peer-reviewed journal. A number of multifrequency high-frequency (HF) radar-based studies to measure upper ocean shear have been conducted [e.g., *Fernandez et al.*, 1996; *Teague et al.*, 2001]. MRs have the advantage that they sample the ocean wave spectrum over lengths from $\sim$20 to several 100 m, whereas HF radars sense-specific wave numbers depending on their operating frequencies.

This article is organized as follows: much of the theoretical background for this work was developed in the 1970s and 1980s, when first attempts were made to measure near-surface vertical current shear using HF radar [e.g., *Stewart and Joy*, 1974; *Ha*, 1979]. Section 2 builds on these findings, as it explains how MR currents can be decomposed into filtered Stokes and quasi-Eulerian components. It also defines the effective depth of the radar-derived currents, and reviews the existing literature on wind and wave-driven flow. This study uses data that were collected from R/V *Roger Revelle* during the Impact of Typhoons on the Ocean in the Pacific (ITOP) field campaign in 2010. Section 3 gives an overview of the ITOP data set, and discusses the wave modeling techniques employed to support our results. The near-surface vertical current shear retrieval methodology is introduced in section 4. It focuses on the newly developed processing steps necessary for determining shear, and discusses similarities and differences with the standard single current vector retrieval technique by *Young et al.* [1985b] and *Senet et al.* [2001]. Section 5 presents first MR near-surface vertical current shear measurements. Results are put in context with the wind and wave forces driving the shear, as well as the large-scale upper ocean circulation in the area. The section also provides evidence of near-surface Ekman dynamics, which is compared with drift parameters (i.e., speed factor and deflection angle) from the scientific literature. The article closes with conclusions and directions for future research (section 6).

2. Background

2.1. Filtered Stokes and Quasi-Eulerian Currents From Radar

To retrieve the near-surface current from MR backscatter data, one must measure the phase velocity of the imaged surface gravity waves. That measurement's deviation from the still water dispersion relationship yields the desired current vector. A measure of the same parameter is obtained with a pair of HF radars. The Doppler frequency shifts of the dominant peaks within a HF radar sea echo spectrum yield the phase speed of the Bragg-resonant ocean waves moving toward or away from the radar. (At grazing incidence, the Bragg waves have half the wavelength of the radar electromagnetic waves—for example, a 12.4 MHz system senses Bragg waves with a length of 12.1 m.) In order to obtain the total current vector, two spatially separated HF radar units must be employed [*Barrick et al.*, 1977]. To determine an accurate current vector, both radar systems require significant directional wave spreading, which is generally fulfilled under natural sea states [e.g., *Rogers and Wang*, 2007]. The theoretical background that has been developed for HF radar currents thus equally applies to MR.

Following *Ardhuin et al.* [2009], the radar-derived current $\mathbf{U}_R(k_D)$ can be represented as a superposition of a quasi-Eulerian current $\mathbf{U}_E(k_D)$ [*Stewart and Joy*, 1974; *Kirby and Chen*, 1989] and a wave-induced current $\mathbf{U}_{Sf}(k_D)$:

$$\mathbf{U}_R(k_D)=\mathbf{U}_E(k_D)+\mathbf{U}_{Sf}(k_D). \tag{1}$$

The radar-derived current is always a function of the ocean wave number k_D from which it is derived, but to simplify notation the variable will be omitted in what follows. $\mathbf{U}_{Sf}$ is due to a nonlinear correction term to the linear wave phase velocity [*Weber and Barrick*, 1977] that can be interpreted as a filtered surface Stokes drift [*Ardhuin et al*., 2009]. $\mathbf{U}_E$ is a combination of tidal currents, pressure-driven (geostrophic) currents, inertial motions, and wind drift. From the nonlinear correction term given by *Weber and Barrick* [1977], it has been shown [*Broche et al*., 1983; *Ardhuin et al*., 2009] that the filtered Stokes drift affecting the radar-derived currents can be approximated by:

$$U_{Sf}(k_D, \theta_D) \simeq \mathbf{U}_{SS}(f_D) \cdot \mathbf{e}_{\theta_D} + 4\pi k_D \int_{f_D}^{\infty} \int_0^{2\pi} f \cos(\theta - \theta_D) E(f, \theta) \mathrm{d}\theta \mathrm{d}f, \tag{2}$$

where θ_D and f_D are the direction and frequency of the ocean waves on which the estimates are based, and $\mathbf{e}_{\theta_D}$ is the unit vector directed toward θ_D. The expression is dominated by $\mathbf{U}_{SS}$, which is the Stokes drift vector for waves with frequencies up to f_D:

$$\mathbf{U}_{SS}(f_D) = 4\pi \int_0^{f_D} \int_0^{2\pi} f \mathbf{k}(f) E(f, \theta) \mathrm{d}f \mathrm{d}\theta. \tag{3}$$

Here $E(f,\theta)$ is the directional wave spectrum and $\mathbf{k}$ the wave number vector. According to the linear dispersion relationship for deep water waves, the latter is given by $(2\pi f)^2/g$, where g is the acceleration due to gravity. While the expression for $U_{Sf}(k_D, \theta_D)$ cannot be exactly given by the projection of a vector $\mathbf{U}_{Sf}$ in direction θ_D, *Ardhuin et al*. [2009] argue that this is a reasonable approximation.

2.2. Effective Depth of Currents

The effective depth of the quasi-Eulerian current $\mathbf{U}_E$ was first investigated by *Stewart and Joy* [1974] using linear wave theory. Assuming deep water and a current that is small compared with the wave phase speed, they found that:

$$\mathbf{U}_E(k_D) = 2k_D \int_0^h \mathbf{U}(z) \exp(-2k_D z) \mathrm{d}z. \tag{4}$$

Here $\mathbf{U}(z)$ is the vertical current profile with z positive downward and h is the water depth. The solution shows that $\mathbf{U}_E$ represents a weighted average of the current from the surface down to the penetration depth of the wave, which is approximately half the ocean wavelength $\lambda_D = \frac{2\pi}{k_D}$ sensed by the radar [*Dean and Dalrymple*, 1991]. The relative contributions to $\mathbf{U}_E$ are greatest at the surface and decrease exponentially with depth as $\exp(-2k_D z)$. As a result, the effective depth of $\mathbf{U}_E$ increases with λ_D. For the special case of a linear current profile, it can be shown analytically that the radar-derived current corresponds to an effective depth of 7.8% of λ_D [*Ha*, 1979]. For a logarithmic profile, the effective depth is 4.4% of λ_D. A finite water depth counterpart to equation (4) has been found by *Kirby and Chen* [1989].

The present study exploits the fact that longer ocean waves are affected by currents at greater depths than shorter waves. Since our MR data were acquired in deep water (see section 3 for details), it is based on *Stewart and Joy*'s [1974] solution (equation (4)). Since their theory neglects higher-order terms, the filtered Stokes drift $\mathbf{U}_{Sf}$ needs to be subtracted from the radar-derived $\mathbf{U}_R$ to determine $\mathbf{U}_E$. This requires knowledge of the directional wave spectrum $E(f,\theta)$ (see equations (1) and (2)). When assigning an effective depth to our measurements, we assume a linear current profile. This assumption is common in the literature [e.g., *Ullman et al*., 2006], but it is of course a simplification. For a general current profile, the effective depth of the radar measurements depends on both the current profile's shape and λ_D. Thus, determining the near-surface current profile $\mathbf{U}(z)$ would require the inverse solution of equation (4). *Ha* [1979] proposed a stabilized numerical inversion method that yielded reasonable results for HF radar observations, although sensitive to measurement noise. He concluded that results could be improved if a larger number of radar frequencies were available, since that would reduce random errors in the measurements. The numerical inversion of MR currents to obtain $\mathbf{U}(z)$ will be addressed in a future work.

2.3. Wind and Wave-Driven Currents

Ekman's [1905] theory explains steady wind-driven currents in an infinite homogeneous ocean. It assumes a momentum balance between the Coriolis force due to the Earth's rotation and the shear stresses exerted by the wind on the ocean. The downward transfer of momentum is achieved by a turbulent stress, for which a constant eddy viscosity is assumed. Ekman theory predicts a surface current that is proportional to the wind stress and lies 45° to its right (in the Northern Hemisphere, assumed throughout). With increasing depth, the current rotates to the right and its speed decreases. The resulting vertical velocity profile has a spiral structure (the so-called Ekman spiral).

However, Ekman's theory does not account for the presence of surface waves, which profoundly modify the ocean surface layer [e.g., *Sullivan et al*., 2007; *McWilliams et al*., 2012; *Tamura et al*., 2012]. *Lewis and Belcher* [2004] show that the wave-induced Stokes drift is key to understanding near-surface current profile observations. The Stokes drift is strongly sheared, decaying rapidly away from the surface. It is dominated by the high-frequency part of the wave spectrum, which is due to the $f\mathbf{k}$ term in equation (3). Hence, the relatively short wind waves generally have a greater influence on the Stokes drift than long swell. Based on 12.5 MHz HF radar measurements off the west coast of France and WAVEWATCH III (WW3) modeling results, *Ardhuin et al*. [2009] find that U_{Sf} is on the order of 0.5%–1.3% of U_{10}, generally exceeding the wind drift which is on the order of 0.6% of U_{10}. A common Stokes depth scale (i.e., the depth down to which the Stokes drift remains important) is 5 m [*Polton et al*., 2005]. This is significantly shallower than the typical Ekman layer depth scale of 30 m [*Price et al*., 1987].

While surface flow to the right of the wind has been observed, its structure is complex and rarely consistent with Ekman's predictions [e.g., *Schudlich and Price*, 1998; *Ralph and Niiler*, 1999; *Yoshikawa et al*., 2007]. This is because the real (i.e., nonidealized) near-surface current profile $\mathbf{U}(z)$ depends on a host of spatially and temporally varying factors, including wind stress, diurnal heating and cooling, and surface waves. Based on long-term time-averaged observations, *Lewis and Belcher* [2004] list three main features of the steady state mean current: (1) a surface current at an angle of 10°–45° to the right of the wind; (2) at depths from $\sim$5 to 20 m, currents are deflected by $\sim$75°; (3) the magnitude of the current rapidly attenuates below the surface. In the present paper, we will compare our MR near-surface vertical current shear observations with these general characteristics.

3. Data Overview

The results presented here are based on measurements that were made during an extensive field campaign in the Philippine Sea in 2010, as part of the ITOP program [*D'Asaro et al*., 2014]. Our focus lies on MR data that we collected from R/V *Roger Revelle* during four separate cruises (RR1010, RR1012, RR1014, and RR1015) covering a total of 26 days, spanning from August to October 2010. Figure 1a shows a map of the study area with cruise tracks and bathymetry [*IOC et al*., 2003]. During ITOP, the *Revelle* was based in Kaohsiung, Taiwan. As part of the program, two Air-Sea Interaction Spar (ASIS) and Extreme Air-Sea Interaction (EASI) buoy pairs were deployed east of Taiwan, at 21.28°N, 126.88°E (in 5450 m depth) and 19.68°N, 127.38°E (5500 m) [*Graber et al*., 2000; *Drennan et al*., 2014]. Figure 1b shows a picture of the *Revelle* with an ASIS-EASI buoy pair in the foreground.

The *Revelle* is equipped with two 9.4 GHz (X-band) HH-polarized (i.e., horizontal transmit and receive) noncoherent MRs, a standard navigational one and a dedicated science system. Both are located on the ship's main mast, operating at grazing incidence. The science MR is a Furuno FAR2117BB with an 8 foot antenna (i.e., a horizontal beam width of 0.75°), an antenna rotation period of $\sim$1.4 s, and a pulse repetition frequency of 3 kHz. It was set to operate at a pulse length of 0.07 μs (i.e., a range resolution of 10.5 m). The MR is connected to a computer with a Wave Monitoring System (WaMoS) by OceanWaveS. WaMoS digitizes the logarithmically compressed video signal from the radar, keeping track of the antenna look direction for each sampled pulse. The radar images are analyzed in near-real time to provide wave and current information [*Dittmer*, 1995; *Ziemer*, 1995]. WaMoS was set to store the radar return from the sea surface over a range from 247.5 to 2152.5 m at a sampling frequency of 20 MHz (i.e., a range cell size of 7.5 m). On average, WaMoS sampled $\sim$1/3.5 microwave pulses, resulting in an azimuth cell size of $\sim$0.3°. (It would have been preferable if the system had sampled all pulses, but this was not possible at the time due to hardware limitations, an issue that has since been resolved by OceanWaveS.) The radar return measured by WaMoS is not radiometrically calibrated, with backscatter intensity values ranging from 0 to 4095 (i.e., a 12 bit image depth).

Here the WaMoS raw polar radar images were postprocessed using IDL-based software developed at the University of Miami, but shipboard analysis in near-real time is possible. The analysis was carried out on a computer equipped with 48 GB memory and eight 2.8 GHz processors. An example of a MR image from the *Revelle* is shown in Figure 1c. An aft portion of the radar field of view (FOV) has reduced backscatter due to the main mast's shadow. This region will be disregarded in the following analysis.

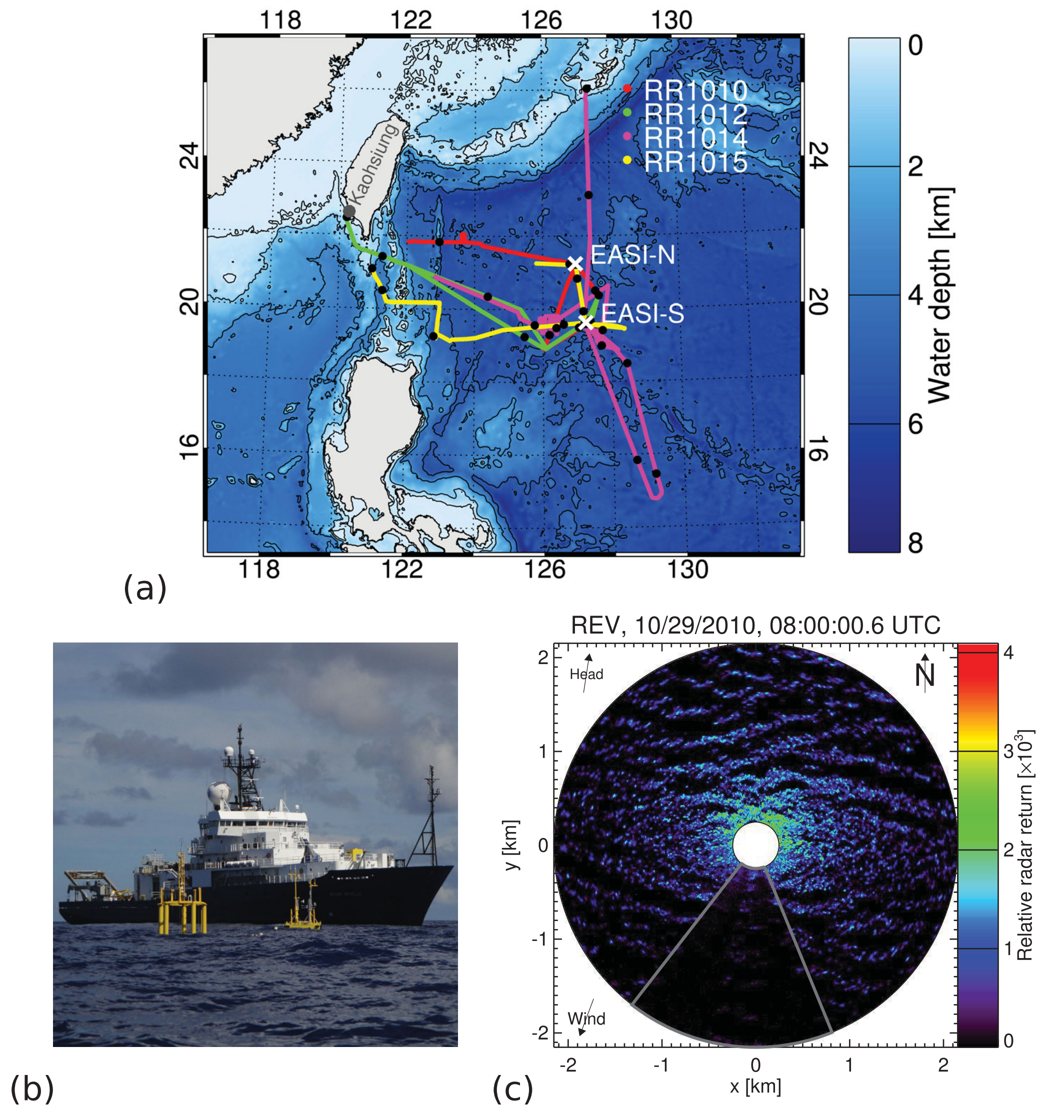

Figure 1. Map of R/V *Roger Revelle* cruise tracks and bathymetry from the GEBCO Digital Atlas. The black dots on the tracks indicate the passage of 1 day. (a) ASIS-EASI mooring sites are given by white crosses. (b) Picture of the *Revelle* during ITOP with an ASIS-EASI pair in the foreground. Radar image acquired from the *Revelle* on 29 October 2010, 08:00 UTC. (c) The gray image slice marks the area that is shadowed by the ship's main mast.

We use shipboard ADCP data as a reference for our MR measurements. The *Revelle* has two ADCPs mounted on its hull, an Ocean Surveyor 75 kHz (OS75) and a Narrowband 150 kHz (NB150), both manufactured by Teledyne RD Instruments. Here we use the NB150, which is better suited for upper ocean studies. Depending on its mode of operation, NB150s depth bins range from 21 to 413 m in 8 m increments or from 19 to 215 m in 4 m increments. The University of Hawaii Data Acquisition System (UHDAS) acquires the ADCP data and processes them using the Common Ocean Data Access System (CODAS) [*Firing and Hummon*, 2010].

Accurate heading information that is correctly aligned with the current sensor is key to reliable shipboard current measurements. This is well established within the shipboard ADCP community [*Firing and Hummon*, 2010], but has only recently been demonstrated for MR current retrieval from ships [*Lund et al.*, 2015b]. A bias of only 1° in the ship heading puts an error of 1.7% of the ship speed in the current estimate's cross-track component, i.e., an error of 0.10 m s^{-1} at the *Revelle*'s transit speed of 6.0 m s^{-1}. To minimize ship motion related errors, heading information is obtained from both a Sperry MK 37 MOD D/E gyro compass and an Ashtech ADU-2, a multiantenna carrier-phase differential GPS (offering a heading accuracy of 1 mrad). A Trimble GPS receiver provides ship position data. For details on the MR heading correction and "calibration" technique, the reader is referred to *Lund et al*. [2015b].

To determine how the near-surface vertical current shear is affected by the wind, we use measurements from two shipboard anemometers. The primary wind sensor is a R.M. Young Ultrasonic 85000 in a well-exposed location on the meteorological mast on the bow of the ship at a height of 17 m. The secondary wind sensor is a R.M. Young 5300 "airplane," located on the main mast at a height of 25 m. The primary sensor failed during RR1014 on 22 October 2010, around 23:00 UTC, and remained nonfunctional throughout RR1015. An iterative approach was used to correct the wind speeds to 10 m above sea surface (U_{10}), with friction velocity and drag coefficient computed according to *Smith* [1980], assuming neutral conditions.

A third-generation wave model, WW3 version 3.14 [*Tolman*, 2009], is used to evaluate the influence of the Stokes drift on our measurements. We employed a nested model domain for grid resolutions of 0.3° (outer nest) and 0.1° (inner nest). The outer nest covers the Pacific excluding the polar regions (66°S–69.3°N and 98.5°E–293.2°E). The inner nest is used to investigate the wavefields in the northwestern Pacific (11.6°S–41.5°N and 98.7°E–130.5°E). The hindcast was performed over the entire year of 2010 for the outer nest, and from July to November for the inner nest. The wave model is driven by 6 hourly surface winds from the National Centers for Environmental Prediction/Climate Forecast System Reanalysis (NCEP/CFSR) product [*Saha et al*., 2010]. Equation (2) is used to determine the filtered Stokes drift from WW3 directional wave spectra. (To validate the WW3 model results, they were compared with Stokes drift estimates from the EASI buoy wave measurements. To this end, we followed *Ardhuin et al*. [2009] by computing the nondirectional Stokes drift $U_{SSnd}(f_D)=2(2\pi)^3 m_3 f_D/g$ for both model and buoys. The third moment of the wave spectrum is given by $m_3=\int_0^{f_D} f^3 E(f)\mathrm{d}f$. At both buoy locations, the correlation coefficient is 0.91, the standard deviation $\sim$0.03 m s^{-1}, and WW3 is biased high by $\sim$0.03–0.04 m s^{-1}, suggesting an overall good WW3-EASI agreement. For details on EASI wave measurements refer to *Collins et al*. [2014].)

4. Methodology

4.1. Backscatter Ramp Correction

The MR backscatter ramp represents the mean radar return as a function of range and antenna look direction. The mean backscatter intensity, essentially a measure of the sea surface roughness, strongly correlates with the wind speed [*Lund et al*., 2012]. For HH-polarized systems as used here, a single backscatter intensity peak is observed upwind. The backscatter intensity furthermore exhibits a rapid decay with range. According to theory, the radar return should be inversely proportional to the third power of range R. But because the video signal passes through a logarithmic amplifier before it is captured by WaMoS, and the exact form of the Furuno amplification function is unknown, the R^{-3} proportionality is not strictly valid [cf. *Gommenginger et al*., 2000].

Subtracting the radar backscatter ramp from a sequence of radar images is equivalent to demeaning and detrending the data, which prepares them for the subsequent Fourier analysis. Traditionally, the near-surface current analysis is performed over windows covering only a small portion of the radar FOV (e.g., 128 $\times$ 128 pixels with 7.5 m resolution). Within such windows, the variability of the backscatter intensity with range and azimuth is limited. Hence, the usual approach is to simply subtract the overall spatiotemporal mean from the radar image sequence [e.g., *Nieto Borge and Guedes Soares*, 2000]. But here the entire FOV is analyzed, which is why we need to account for the radar return's range and azimuth dependency. The main reason for analyzing the entire FOV is to remove biases toward waves traveling along the line of sight between radar and analysis window [*Lund et al*., 2014]. Analyzing the entire FOV improves current retrieval results by making waves detectable over a broader range of directions.

Since the response of the MR backscatter ramp to changing wind conditions (and other environmental parameters) is still incompletely understood, we define the ramp empirically. To this end, a sequence of MR images is temporally averaged and downsampled (in range and azimuth). The temporal mean image could carry a signal (albeit weak) that interferes with the wave signatures. Therefore, we define a "smoothed" ramp by least squares fitting a Fourier series to the backscatter dependency on azimuth. This is done repeatedly for all ranges. The advantage of a Fourier fit over a sliding window average is that it allows us to disregard shadowed antenna look directions without having to address edge effects. The backscatter ramp is built from the best fit, employing interpolation techniques to recover the original range resolution.

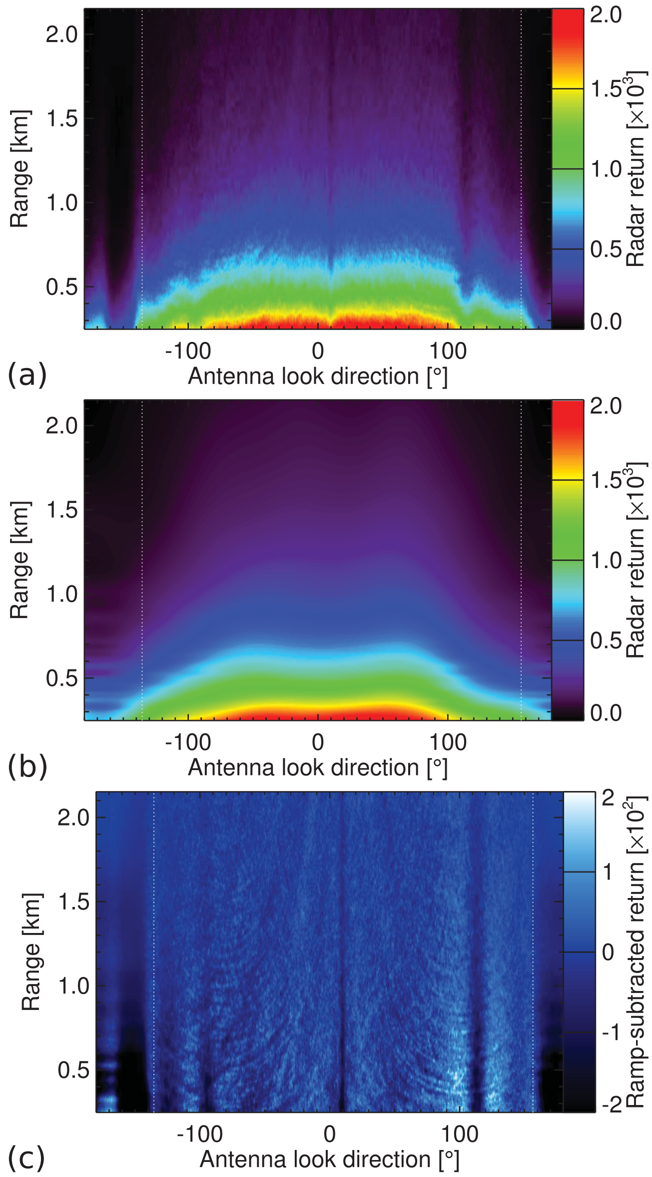

Figure 2. (a) Radar image in polar coordinates, averaged over 12 min, collected from the *Revelle* on 29 October 2010, starting 06:20 UTC. (b) Corresponding radar backscatter ramp, obtained by fitting Fourier curves to the mean radar return. (c) Image of the homogenized, ramp-subtracted mean radar return. The dashed lines delineate the shadowed portion of the radar FOV.

Figures 2a–2c illustrate the radar backscatter ramp correction for 12 min of data collected from the *Revelle* on 29 October 2010, starting at 06:20 UTC. Over this period, the ship anemometer measured a mean wind of 9.0 m s^{-1} coming from 12°. The range decay and upwind peak are evident in Figures 2a and 2b, which show the mean radar return and the corresponding fitted backscatter ramp, respectively. Figure 2c shows the difference between the mean image and its ramp. The difference image is much more homogeneous, revealing linear features (curved in polar coordinates) that may be due to the converging and diverging surface currents associated with Langmuir cells. Figures 2a and 2c have reduced backscatter at antenna look directions greater than ~160° and less than ~−140°. This is the shadow due to the main mast. Less pronounced shadows can be observed at 10° (due to the meteorological mast) as well as around 115° and −95° (due to communication and navigation antennas).

4.2. Pulse-by-Pulse Georeferencing and Trilinear Interpolation

The standard MR current retrieval method treats individual radar images like photographic "snapshots," essentially assuming that both radar platform (in our case the *Revelle*) and target (the sea surface) are stationary during one antenna rotation period [*Young et al*., 1985b; *Senet et al*., 2001]. This is reasonable if the analysis is limited to a small window within the radar FOV. Here we analyze the whole FOV, and the snapshot simplification would ensue significant mapping errors. This is because waves may move across several WaMoS range resolution cells during the ~1.4 s it takes to acquire a radar image. Horizontal ship motion and heading changes would add errors. For example, a 1° heading change during an antenna rotation would lead to a mapping error of 37.6 m at maximum range. Another issue with the standard MR current retrieval method concerns its use of platform-based coordinates, i.e., on ships the analysis windows are positioned at a constant range and angle relative to the bow. A change in ship speed or direction during a measurement period will smear the spectral wave signal, ruling out an accurate current retrieval.

To eliminate the aforementioned problems, we forgo both the snapshot simplification and the platform-based reference frame. Instead, we georeference our radar backscatter data on a pulse-by-pulse basis, i.e., we estimate the antenna look direction and horizontal ship position associated with every single radar pulse. To this end, we use high-resolution (1 s) position data from the ship's GPS receiver, as well as heading

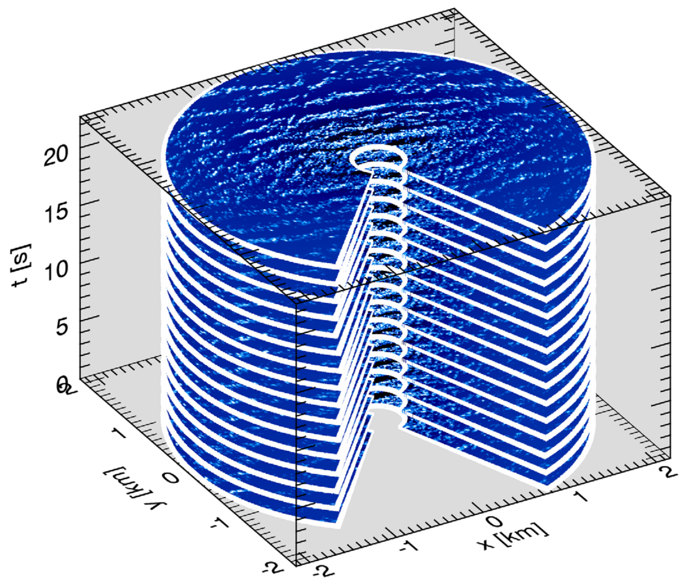

Figure 3. Example of ramp-corrected and interpolated radar backscatter intensity data in space-time coordinates. The figure covers 16 full scans of the sea surface that were collected from the *Revelle* on 29 October 2010, starting 06:20 UTC.

measurements from the gyro compass and the more accurate Ashtech system [*Lund et al.*, 2015b]. For each antenna rotation, WaMoS stores a single time stamp that corresponds to the first radar pulse. We use linear interpolation techniques to first estimate the time at which each radar pulse was acquired, and then the corresponding ship heading as well as position. (The heading of each radar pulse relative to the ship is obtained from the binary bearing signal reported by WaMoS.) Equipped with this information, we trilinearly interpolate the raw polar backscatter data to Cartesian coordinates, accounting for each polar grid point's geographic location and time. The output grid size, we chose for this operation matches the WaMoS range resolution in space and the mean antenna rotation period in time. In the future, we also plan to account for the ship's pitch and roll, which could be done using a conventional inertial measurement unit [*Hill*, 2005].

Figure 3 illustrates a sequence of 16 ramp-corrected radar images after pulse-by-pulse georeferencing and trilinear interpolation, collected on 29 October 2010, 06:20 UTC when the *Revelle* was at station. In transit (i.e., traveling at ~6.0 m s^{-1}), the *Revelle* may cover a distance of ~4.3 km over one measurement period (here 512 complete scans of the sea surface, or ~12 min). In such case, the radar FOV from the beginning and end of a measurement period will barely overlap geographically. To address this issue, we use images of 1024 × 1024 pixels (i.e., 7.68 × 7.68 km; the maximum range of the MR data used here is ~2.15 km), centered around the ship's position in the middle of each measurement period. Data points that lie beyond radar range are filled with zeros. Thus, when interpreting our near-surface vertical current shear results, it is worth noting that they are spatiotemporal averages covering areas that are larger when the ship is underway than when it is stationary.

4.3. From Three-Dimensional Spectral Density to Signal-to-Noise Ratio

A three-dimensional fast Fourier transform (3-D FFT) is employed to convert the georeferenced and trilinearly interpolated ~12 min long image sequences (covering the whole radar FOV) to the wave number-frequency domain. The wave signal within the positive frequencies of the 3-D power density spectrum (or periodogram) is located on a surface that resembles an inverted cone, the dispersion shell. It is defined by the linear dispersion relationship:

$$\omega=\sqrt{gk \tanh kh}+\mathbf{k}\cdot\mathbf{U}, \tag{5}$$

where ω is the angular frequency and $k=|\mathbf{k}|$ the wave number magnitude. For an illustration of the 3-D dispersion shell refer to, e.g., *Lund et al.* [2015b].

The MR near-surface vertical current shear retrieval hinges on the identification of the surface wave signal within the wave number-frequency spectrum. The goal is to identify the wave signal over a broad range of frequencies and directions $\theta=\arctan(k_y, k_x)$, where $k_{x,y}$ are the wave number's x and y component. The standard method to accomplish this involves a power threshold [*Senet et al.*, 2001]. All spectral coordinates that have power above the threshold are attributed to the waves. Under the assumption of a vertically uniform near-surface flow, a single current vector is obtained by minimizing the dispersion shell's distance from these coordinates [*Young et al*., 1985b]. Best results are obtained through an iterative approach that accounts for higher harmonics and temporal aliasing [*Senet et al*., 2001].

The disadvantages associated with using a simple power threshold to identify the wave signal are twofold: (1) the selected spectral coordinates tend to cluster around the peak wave signal, with relatively little spread in direction and frequency; (2) they are biased toward low wave numbers and frequencies, which is due to the background noise characteristics (see below). Here these issues are circumvented by converting the 3-D power density to a signal-to-noise ratio (SNR) spectrum.

To this end, we must quantify the background noise. In the standard method (which uses small rectangular analysis windows at fixed locations relative to the ship), this has been hindered by its complicated elliptical shape, depending on θ, k, and ω. The θ-dependency is due to the fact that the range resolution (here 10.5 m) is typically higher than the azimuthal resolution (0.75°, e.g., ~28 m at maximum range) [*Seemann et al*., 1997]. As a result, the spectra have greater variance in range than in azimuth. By analyzing the whole radar FOV, all directions face the same measurement constraints. The background noise thus becomes a function of k and ω only, facilitating our task considerably.

We proceed as follows: first, the iterative least squares regression algorithm by *Senet et al*. [2001] is employed to obtain an estimate of the mean near-surface current $\overline{\mathbf{U}}$ (representative of the upper ~6 m, according to *Young et al*. [1985a]). With this knowledge at hand, we repeat the pulse-by-pulse georeferencing and trilinear interpolation outlined in the previous subsection, but now the reference frame moves with velocity $\overline{\mathbf{U}}$. If the near-surface flow is vertically uniform, the surface wave signal, once transformed to wave number-frequency space, will lie on the perfectly symmetric still water dispersion shell. The moving reference frame has the advantage that it reduces aliasing, which may lead to ambiguities in the selection of spectral coordinates for the current estimates. It also facilitates the current shear retrieval in that it keeps the wave energy at any given frequency within a narrow range of wave number magnitudes (see section 4.4). Second, we transform the 3-D spectrum to polar form and integrate over the half of the spectrum (in terms of θ) which is characterized by the lowest standard deviation over k. This is done to minimize wave contributions and associated nonlinearities. The background noise's dependency on k and ω is obtained from a filtered (and smoothed) version of this integral. The fundamental mode wave energy located along the dispersion curve, as well as spectral coordinates near the zero-frequency and wave number, are masked and filled by interpolation from neighboring data points.

To illustrate this process, Figures 4a and 4b show diagrams of mean spectral density as function of k and ω for ~12 min of data (collected on 29 October 2010, starting 06:20 UTC). The former corresponds to the half of the spectrum with the highest standard deviation over k, the latter represents the half with the lowest standard deviation. Figure 4a shows prominent peaks along the still water fundamental mode dispersion curve (equation (5)), first, and second harmonic, as well as the so-called group line [e.g., *Smith et al*., 1996]. (The higher harmonics appear mainly due to the nonlinearity of the MR imaging mechanism, especially shadowing effects, with nonlinearities of the sea state itself playing only a secondary role [*Seemann et al*., 1997]. The physical origin of the group line is not yet clear, but it has previously been attributed to wave groups [*Smith et al*., 1996] and breaking waves [*Stevens et al*., 1999].) In Figure 4b, no higher harmonic or group line contributions can be discerned, i.e., they are limited to the high-standard-deviation half of the spectrum. The fundamental mode energy is greatly reduced, but still clearly present. This indicates that the wave energy spreads over more than 180°. Figure 4c shows the background noise. It is essentially a filtered version of Figure 4b. The background noise can be seen to decrease with both increasing frequency and, to a greater extent, wave number (note the logarithmic color scale). The SNR that results if we divide the unfiltered power density (Figure 4a) by the background noise is shown in Figure 4d. The fundamental mode wave signal stands out much more clearly in the SNR than in the power density diagram. In addition to the first and second harmonic, we can also identify a third harmonic contribution, though barely.

In the following, we divide our 3-D power density spectra by the (azimuthally invariant) background noise, determined for each individual spectrum as described above. The resulting 3-D SNR spectra are used to isolate the wave signal, which is key to retrieving current shear. We use the same data as in Figure 4 to exemplify how the use of SNR improves the separation of signal from noise. Figures 5a and 5b show the 3-D spectral coordinates associated with the wave signal as determined by power and SNR thresholding, respectively. Traditionally, the power threshold is set to some fraction of the maximum spectral energy

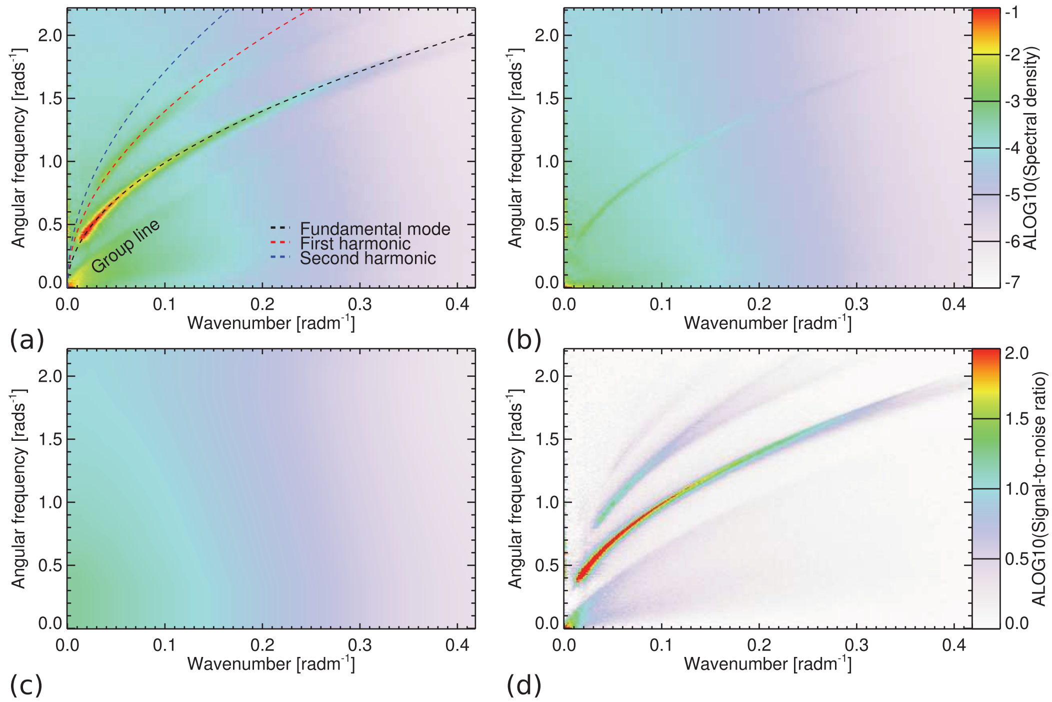

Figure 4. Directionally averaged 3-D spectra obtained from 12 min of *Revelle* data, acquired on 29 October 2010, starting 06:20 UTC. Spectral halves with (a) greatest and (b) lowest frequency-averaged standard deviation of spectral density over *k*. (c) Background noise estimated from spectral half with lowest standard deviation. (d) SNR obtained by dividing the spectral half with the greatest standard deviation by the background noise estimate. The color scale shown in Figure 4b also applies to Figures 4a and 4c; note that both scales are logarithmic.

[*Senet et al*., 2001]. Here it was set to 0.001. Though subjective, we believe that this threshold value was optimally chosen in that it maximizes the number of spectral coordinates located on the dispersion shell while keeping group line or nonwave-related contributions at a manageable level. The SNR threshold was set to a conservative value of 5. The advantages of the SNR-based detection of the wave signal are evident in that it spans over a much greater range of frequencies and directions. Also, group line contributions are less prominent.

4.4. Current Shear Retrieval

To retrieve near-surface vertical current shear from MR image sequences, we exploit the fact that the long ocean waves sense the current at a greater effective depth than the short ones (see section 2.2). This requires a small but significant departure from the standard method by *Young et al*. [1985b] and *Senet et al*. [2001]. Instead of using all spectral coordinates attributed to the surface waves, covering a broad range of wave numbers, we perform the current analysis as a function of wave number. The standard method yields a single current vector per measurement period ($\sim$12 min), ours produces multiple (here, of the order of 100) independent estimates.

The analysis starts with a 3-D SNR spectrum, obtained as explained in the previous subsection. Remember that the frame of reference of the image sequence used to produce the SNR spectrum moves with the radar-derived mean current $\overline{\mathbf{U}}$. Hence, any deviation of the wave signal from the still water dispersion relationship suggests the presence of vertical current shear. The shear retrieval's greatest challenge lies in identifying the wave signal over the widest possible range of wave numbers and directions. To this end, we transform our 3-D SNR spectrum from $\left(k_x, k_y, \omega\right)$ to (k, θ, ω). (This step is also used by *Shen et al*. [2015] within their MR mean current retrieval algorithm.) For any $\langle\theta, \omega\rangle$ pair, just one *k* value may be associated with the surface waves, according to the linear dispersion relationship (equation (5)). We determine the wave number that has the highest SNR for all directions and frequencies, keeping only spectral coordinates where the signal lies significantly above noise level, and that are within a reasonable distance from the dispersion shell (i.e., unrealistic Doppler shifts are discarded). A more precise wave number is estimated from

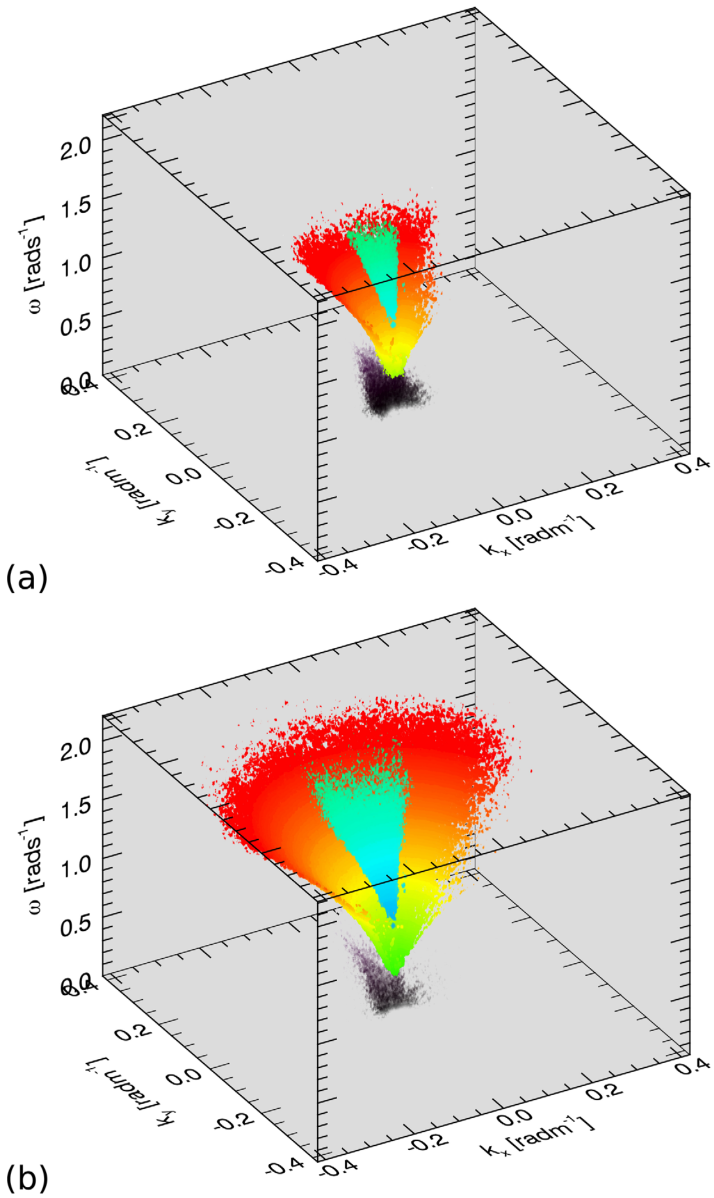

Figure 5. 3-D spectral coordinates associated with surface waves identified by (a) power and (b) SNR thresholding. Coordinates plotted in black-magenta lie on the group line, in yellow-red on the fundamental mode dispersion shell, and in turquoise-green on the first harmonic. The corresponding MR images were acquired from the *Revelle* over ~12 min on 29 October 2010, starting 06:20 UTC.

the peak of a parabola that is fitted through the SNR maximum and the two values on either side of it. (In the future, we plan to further improve the localization of low-wave number components by implementing *Bell and Osler*'s [2011] phase locked loop algorithm.) This approach represents another departure from the standard method, which uses all coordinates indiscriminately, making the implicit assumption that the waves' spectral coordinates are evenly distributed around the dispersion shell. Here a current vector is determined for each frequency slice containing sufficient wave information using *Senet et al.*'s [2001] iterative least squares regression algorithm. Each spectrum has 257 frequency slices, ~100 of which typically yield a reliable current. We also retain a mean SNR (obtained by averaging the SNR along the dispersion curve, accounting for the measured Doppler shift) and wave number (obtained by averaging the wave number magnitude of all coordinates used in the current fit's final iteration) value associated with each current vector.

As an example, Figure 6 shows MR currents as a function of wave number and effective depth (assuming a linear profile, see section 2.2). They are based on ~12 min of data collected from the *Revelle* on 29 October 2010, starting 06:20 UTC. The currents were rotated into the wind, which was coming roughly from north (11°) with a speed of 7.5 m s^{-1}. At the time, the shipboard ADCP's 101 m bin registered a current of $\langle 0.35, 0.17 \rangle$ m s^{-1} in wind and cross-wind (positive direction to the left) direction, respectively. This current is assumed to be the background (i.e., tidal and geostrophic) flow and was subtracted from the radar measurements. The figure also includes the corresponding SNR values, a fifth-order polynomial fit to the MR currents, as well as the WW3-based filtered Stokes drift. The following observations can be made: (1) the assumption of a uniform near-surface flow is indeed, at least in this case, inaccurate. The current speed from the largest to the smallest wave number (i.e., from the shallowest to the greatest effective depth) is reduced by ~25% from 0.32 to 0.24 m s^{-1}. This reduction in speed is accompanied by a clockwise (CW) rotation from 29° to 42° (to the right of the wind). These trends are consistent with what has been reported in the literature (see section 2.3). (2) The filtered Stokes drift, though weaker than the MR

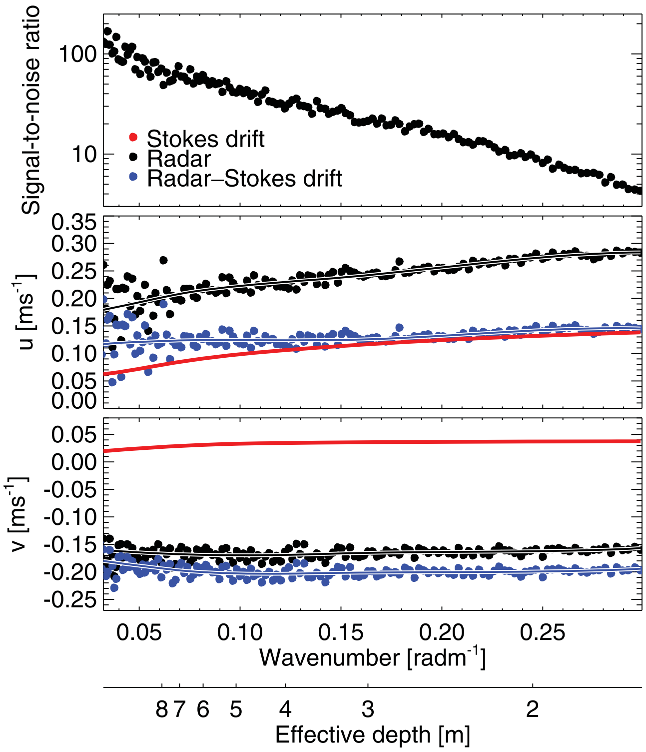

Figure 6. Example of MR near-surface vertical current shear measurements (black points) with corresponding WW3-based filtered Stokes drift estimates (red lines) as a function of wave number and effective depth (assuming a linear current profile). The graph also includes the quasi-Eulerian current (blue points; obtained by subtracting the filtered Stokes drift from the MR results). Data were acquired from the *Revelle* over ~12 min on 29 October 2010, starting 06:20 UTC. The top plot gives the mean SNR along each current estimate's dispersion curve. The middle and bottom plots correspond to the flow components in wind and cross-wind direction, respectively. The black and blue lines give the results of fifth-order polynomial fits to the MR-based currents.

currents, follows a similar trend in terms of speed, decreasing from 0.14 to 0.07 m s^{-1}. It is in a direction slightly to the left of the wind, changing only minimally from $-15°$ to $-17°$. (3) The quasi-Eulerian flow that is obtained by subtracting the filtered Stokes drift from the MR currents has very limited shear. Its speed decays from 0.24 to 0.21 m s^{-1} and its deflection angle (relative to the wind) increases from 53° to 57° with increasing effective depth. Most of the observed near-surface vertical current shear is thus due to the wave-induced Stokes drift. (4) The mean SNR decays exponentially from low to high wave numbers, which is related to the wave energy density spectrum. (The exact form of the transfer function from SNR to wave energy density is unknown.) But even at the largest wave number, which corresponds to the shortest wave we can measure (the minimum wavelength is 21 m, i.e., twice the radar's range resolution), the mean signal is still 4 times greater than the noise floor. The limited scatter in the current estimates from the upper wave number end indicates that an accurate retrieval remains possible despite the relatively low SNR. (5) The MR current estimates for the very low wave numbers exhibit the most scatter. This is due to their reduced sensitivity toward currents, as demonstrated below.

Figure 7 illustrates the accuracy limits of the MR near-surface vertical current shear retrieval. The figure shows the number of wave number resolution cells by which the wave signal gets Doppler shifted for all possible frequencies (from 0 to ω_{Ny}) and current speeds up to 1.0 m s^{-1}. Analyzing the entire radar FOV leads to a finer wave number resolution, improving the method's sensitivity to small current changes. As expected, the Doppler shift is most pronounced for high frequencies and large currents. This is reflected in our results (see Figure 6), which exhibit increased scatter at wave numbers under ~0.06 rad m^{-1} (i.e., an angular frequency of 0.77 rad s^{-1}). In the following, we will limit our analysis to wave numbers above this threshold. In other words, effective depths greater than 8 m will be disregarded. On the high wave number end, SNR may become a limiting factor, especially under low wind and wave conditions. To err on the conservative side, we exclude effective depths shallower than 2 m (in our example, the SNR at 2 m effective depth is ~10). (During the four ITOP cruises reported here, there was a generous supply of swell, hence the low-wave number signal was usually significantly above noise level.)

5. Results and Discussion

5.1. Near-Surface Current Shear Measurements

The quantitative response of the upper ocean flow to wind and wave forcing is still relatively poorly understood. In areas where tidal and geostrophic currents are important, the near-surface and subsurface flows are highly correlated. Elsewhere, surface velocities are largely defined by winds and waves [*Ardhuin et al.*, 2009].

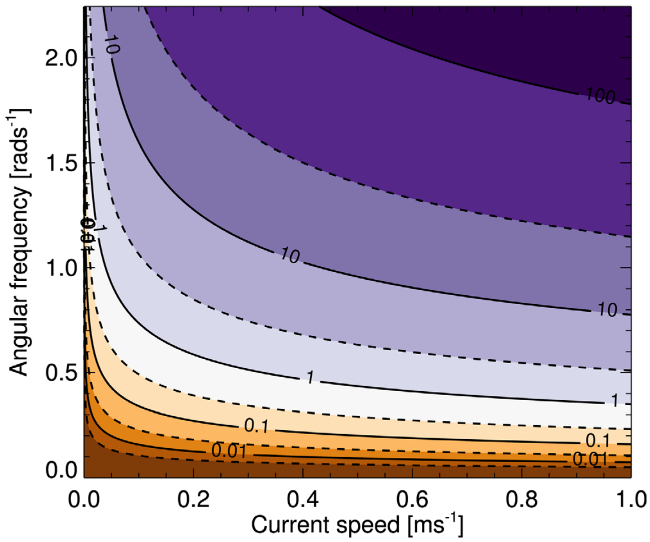

Figure 7. Illustration of the MR retrieval scheme's sensitivity to currents. Contour lines represent the Doppler shift in terms of wave number resolution cells for a given current speed and angular frequency. Results are shown for square images with a 1024 pixel edge length and 7.5 m resolution (i.e., a wave number resolution of ~0.0008 rad m^{-1}).

The Philippine Sea has strong baroclinic tides [e.g., *Jan et al.*, 2008]. Furthermore, typhoons frequently occur in the area, triggering inertial motions. The importance of baroclinic and inertial currents in our study area is evident in current measurements we made at the southern ASIS buoy as well as in a JCOPE-T ocean circulation model study we conducted, which are beyond the scope of this paper. (For details on JCOPE-T, refer to *Miyazawa et al.* [2009] and *Varlamov et al.* [2015].) We therefore expect our MR currents to be controlled by the large-scale circulation, which presents a challenge for isolating the wind and wave-driven components.

Figure 8 shows a time series of MR (0.25 rad m^{-1}, or an effective depth of 2 m) and ADCP (21 m) currents covering all four *Revelle* cruises. The currents are highly variable, manifesting multiple CW rotations and at times exceeding 1 m s^{-1}. As expected, the correlation between the near-surface and subsurface flow is excellent. For 26 days' worth of data (2580 data points), the correlation coefficient and standard deviation between the shipboard MR and ADCP current speeds are 0.94 and 0.07 m s^{-1}, respectively. For current directions, the mean directional difference length is 0.91 with a standard deviation of 27.4°. (The mean directional difference length is the length of the vector mean of the set of unit vectors, each of which is oriented by the difference in angles between the two series; a value of 1 means perfect correlation and 0 means no correlation at all.) Biases are negligible for both speed (0.01 m s^{-1}) and direction (0.8°).

The figure also depicts the physical processes driving the differences between near-surface and subsurface flow, namely winds from the ship anemometers and filtered Stokes drift (0.26 rad m^{-1}) from WW3. Over the four cruises, the *Revelle* experienced several tropical cyclones. The heaviest weather occurred during Typhoon Chaba (late October 2010, RR1015), with winds greater than 15 m s^{-1}. (The WW3 significant wave

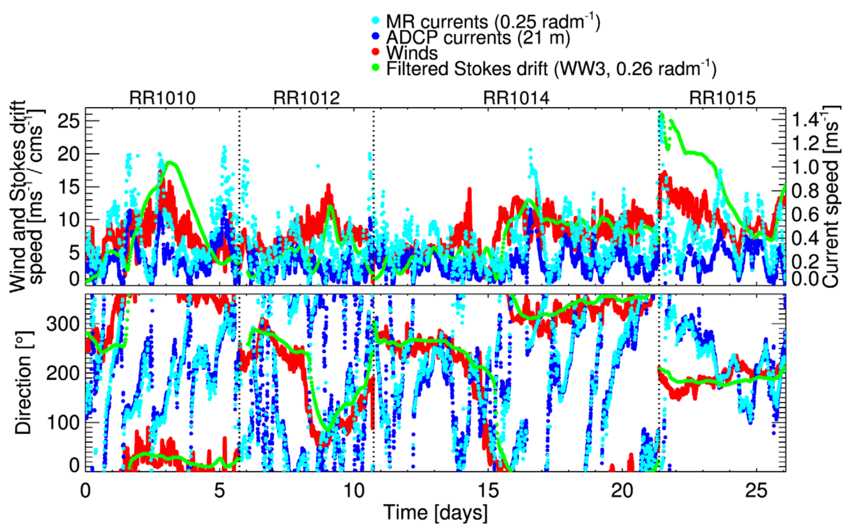

Figure 8. Time series of shipborne winds, ADCP (21 m) and MR (0.25 rad m^{-1}) current measurements, as well as WW3-modeled filtered Stokes drift (0.26 rad m^{-1}) at the *Revelle* location, covering all four cruises. All directions follow the "going to" convention.

height peaked near 8 m.) The filtered Stokes drift reaches values of up to ~0.25 m s^{-1} during Chaba. Its direction generally follows that of the wind, although it occasionally lags behind when the wind turns suddenly, e.g., on days 8–9. There is no discernible agreement between winds and filtered Stokes drift on the one hand and currents on the other, underlining the importance of large-scale processes in our measurements.

The upper ~10 m of the northwestern Pacific are well mixed [e.g., *Jan et al.*, 2008], hence, it is safe to assume that the MR near-surface vertical current shear (covering an effective depth of 2–8 m) is due to the combined action of winds and waves. In the following, we present a selection of MR near-surface vertical current shear measurements. Each three-plot graph in Figure 9 gives five consecutive ~12 min measurements. In total, Figures 9a–9f cover approximately 6 h of MR data. The figures show the azimuthally averaged SNR as a function of wave number as well as the MR current speed and direction over depth, where again a linear profile is assumed (see sections 2.1 and 2.2 for details). The figures also include information on wind and ADCP subsurface (21 m) current velocities at center time (i.e., they correspond to the MR measurements that are plotted as black dots). The SNR in the figures generally decreases exponentially from low to high wave numbers, but it never represents a limiting factor, as confirmed by the excellent MR-ADCP agreement reported above. Wind speeds range from 6.7 to 13.4 m s^{-1} and subsurface currents from 0.03 to 1.08 m s^{-1}. The relative angles between winds and subsurface currents are equally variable, ranging from roughly parallel to counter flow situations. In the cases considered here, the Stokes drift (not shown) is approximately aligned with the wind.

In Figures 9a and 9b, the wind is directed to the right of the subsurface flow, with difference angles of 41° and 26°, respectively. The ADCP-based current speeds of 1.08 (Figure 9a) and 0.25 m s^{-1} (Figure 9b) are large compared with the drift speeds one can expect under the respective 7.1 and 6.7 m s^{-1} winds. (*Madsen* [1977] predicts a speed factor of ~0.03, i.e., the wind drift is 3% of U_{10}; here, this implies surface drift speeds of 21 and 20 cm s^{-1}, which should be considerably reduced at our shallowest effective depth of 2 m.) The MR measurements in both figures indicate a current speed that decreases by ~5 to 10 cm s^{-1} and a current direction that turns by ~5° to 10° counterclockwise (CCW) over effective depths from 2 to 8 m. This shear behavior can be explained by the relative angle between wind and subsurface current: While the radar-derived currents are roughly in the direction of the subsurface flow, they slightly increase in speed and veer in the direction of the wind as the effective depth decreases. Some of the sequential results in both figures are offset relative to each other. This is due to changes in the subsurface current. The fact that the profiles still follow the same trends suggests that the wind and wave forcing remained fairly constant.

Figures 9c and 9d exemplify the opposite case where MR current speeds increase and directions turn CW with increasing effective depth. Again, the results can be explained by examining the shipboard wind and ADCP current measurements. In both figures, winds (and waves) are directed ~125° to the left of the background current. The respective wind speeds are 12.6 and 13.4 m s^{-1}, with subsurface currents of 0.58 and 0.31 m s^{-1}. Under such counter-flow conditions, we expect the currents to decrease in magnitude and veer in the direction of the wind as we get closer to the surface, just as observed.

In Figure 9e, the background current is much weaker than in the previous figures (0.03 m s^{-1}) and the 10.4 m s^{-1} wind (at center time) is almost directly opposed to the background current (171° to its left). The resulting flow decreases in speed from shallow to deep water and is roughly windward throughout. Hence, wind and Stokes drift overpower the background flow. During the full ~1 h period, the subsurface current is turning, under steady wind forcing. As a result, the wind is first to the left and later to the right of the subsurface current. As before, the currents are seen to veer toward the wind and away from the direction of the subsurface current with decreasing effective depth. The current directions at both the first and last time step change by ~90° between depths of 2 and 8 m (although in opposite directions), much more than in the previous figures. This is due to the relatively weak subsurface current, enhancing the role of wind and wave drift.

Finally, Figure 9f illustrates a case of near-surface flow reversal. (The last time step of Figure 9e and the first one of Figure 9f are identical.) The subsurface flow is still weak (0.05 m s^{-1}) and turning under relatively strong (9.3 m s^{-1}) opposing winds (168° to the right), resulting in a great degree of variability in the near-surface current profiles. At center time, the flow is windward from 2 to ~4.5 m, before it reverses and assumes a southerly direction that is roughly aligned with the subsurface current. Accordingly, the current speed first decreases from ~5 cm s^{-1} at 2 m to zero at the point of flow reversal, after which it increases back to about the starting magnitude at 8 m. Thus, wind and Stokes drift first exceed the subsurface current. At ~4.5 m, the

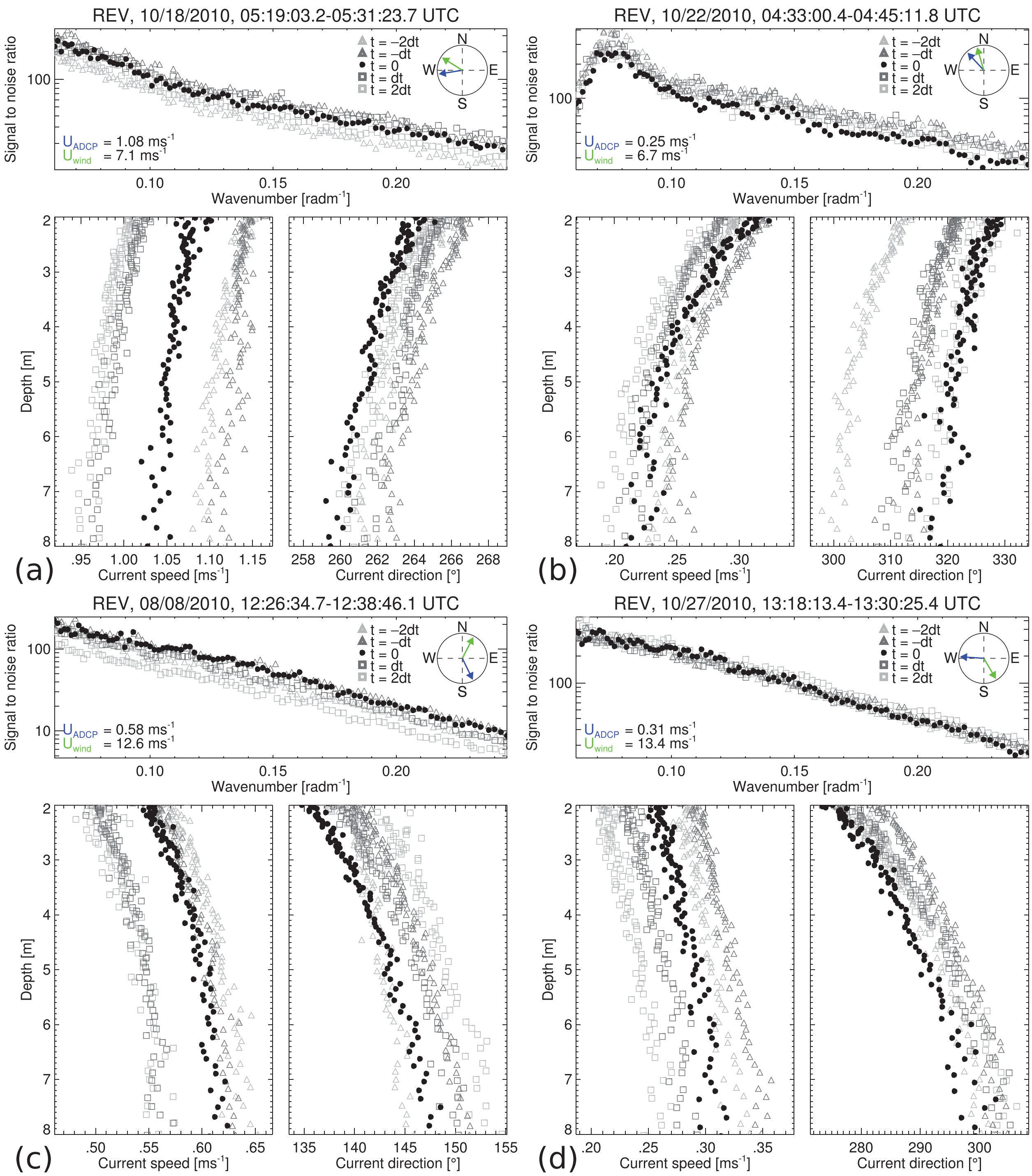

Figure 9. Examples of near-surface current profiles: (a and b) parallel flow with CW forcing, (c and d) counter flow with CCW forcing, (e) parallel flow with transition from CW to CCW forcing, and (f) flow reversal. The effective depth was computed assuming a linear profile. Each graph shows five consecutive measurements, ~12 min apart. The compasses give the wind (green) and ADCP (21 m; blue) current direction at center time, with corresponding radar measurements represented by black dots. The graphs also show the wind and ADCP (21 m) current speed at center time.

wind and wave-induced flow is in balance with the subsurface flow. At greater depths, the forces driving the subsurface flow assume control. A similar flow behavior can be observed at all time steps (except the first), with differences explained by an evolving subsurface current.

Figure 10 provides a more quantitative means of assessing the MR currents' accuracy. It gives the mean absolute difference of the MR measurements from their fifth-order polynomial fit as well as the standard

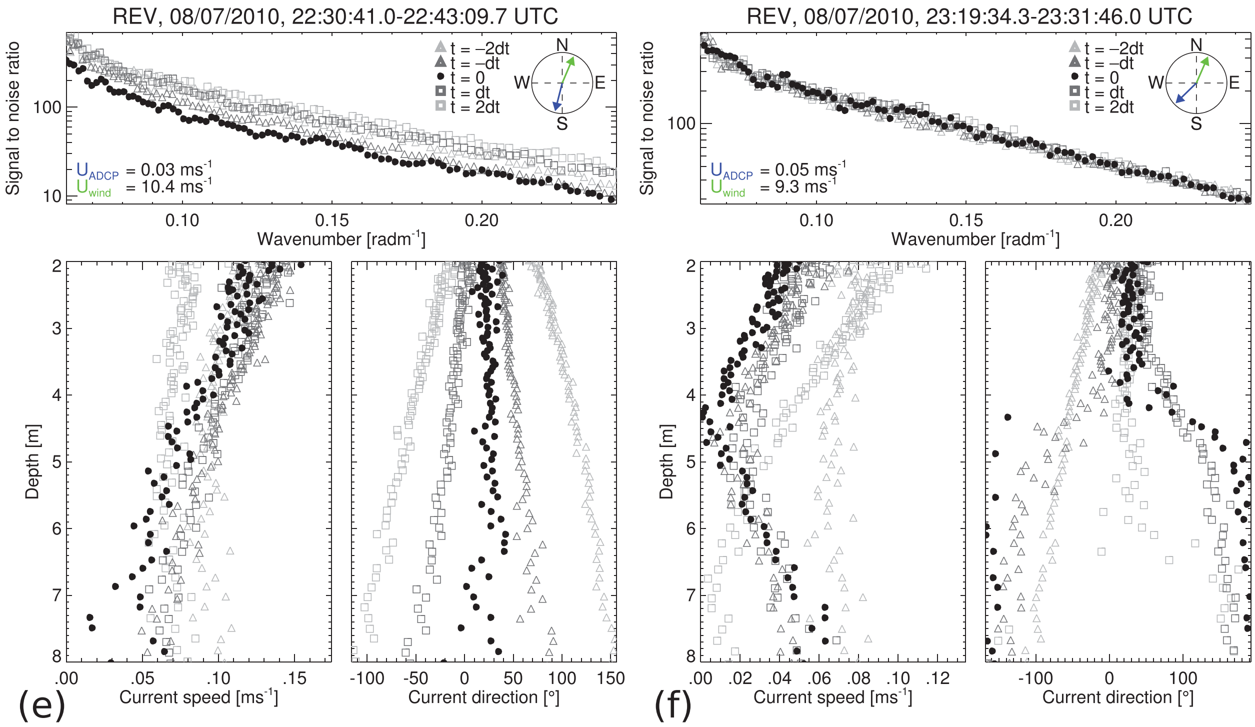

Figure 9. (continued)

deviation of differences as a function of wave number (see section 4.4, Figure 6 for an example of MR measurements with their fitted curves). The MR results are most accurate at ~0.11 rad m^{-1}, with a mean absolute difference of 1.2 cm s^{-1} and a standard deviation of 0.8 cm s^{-1}. Both accuracy measures peak at the lowest wave number (~0.06 rad m^{-1}) with values of 2.5 and 2.3 cm s^{-1}, respectively. On average, the mean absolute difference is 1.5 cm s^{-1} and the standard deviation is 1.2 cm s^{-1}. Since we are lacking near-surface current reference measurements, a definitive conclusion cannot be reached. However, our results are physically consistent with an apparent accuracy on the order of 1–3 cm s^{-1}.

5.2. Evidence of Ekman Dynamics

On average, we expect the wind and wave-induced surface flow to be directed 10–45° to the right of the wind and to decay rapidly with increasing depth [*Lewis and Belcher*, 2004]. But isolating the wind and wave-driven flow is difficult. First, it is generally significantly weaker than the background current (comprising of geostrophic, inertial, and tidal motions), near the measurement error level. Here we make the common assumption that the Ekman flow is more strongly surface trapped than the background current [*Davis et al*., 1981; *Price et al*., 1987]. To obtain an estimate of the wind and wave-driven current, we simply subtract the ADCP-measured current below the greatest expected Ekman layer depth z_r from our MR currents. CTD casts we made at the southern ASIS-EASI site during RR1015 showed that the upper ocean was well mixed down to a depth of ~60 m [*Lund et al*., 2015b]. We therefore chose a z_r value of 100 m (as previously done by *Chereskin and Roemmich* [1991] and *Lenn and Chereskin* [2009]). Second, determining the speed factors and deflection angles (hereafter referred to as drift

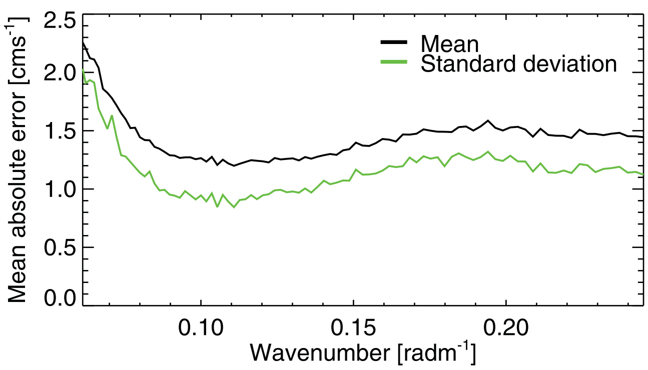

Figure 10. Estimate of the MR near-surface current profile accuracy as a function of wave number. The black line corresponds to the mean absolute difference from fitted polynomial model functions. The green line shows the corresponding standard deviation.

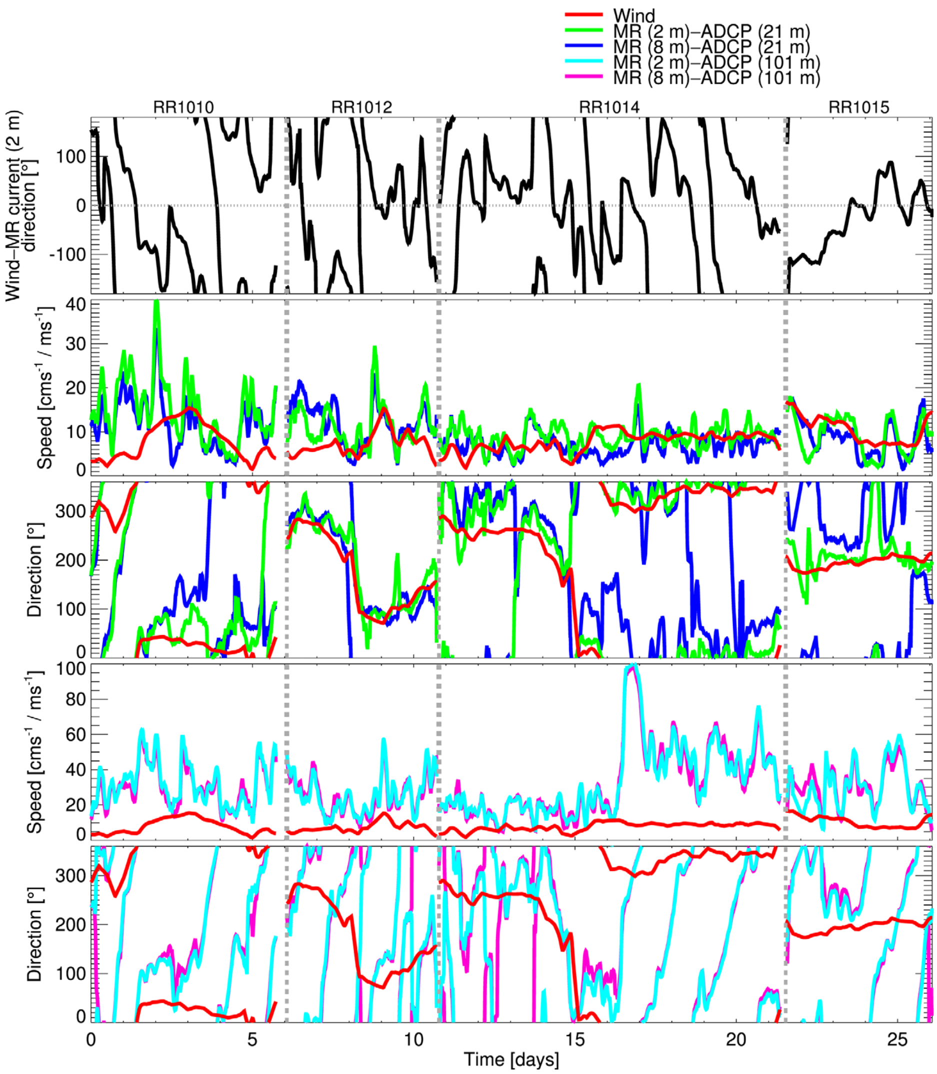

Figure 11. Time series of the MR (2 and 8 m) and ADCP (21 and 101 m) difference currents. The data represent 3 h averages. The 6 hourly NCEP/CFSR reanalysis winds are included for reference. Difference flow speeds are plotted in cm s^{-1} and wind speeds in m s^{-1}. The top plot shows the relative angle between the NCEP/CFSR winds and MR (2 m) currents.

parameters) requires auxiliary wave and wind data, which have errors of their own. We use the filtered Stokes drift from WW3 to estimate the contribution from the waves. Following *Ardhuin et al*. [2009] and *Lenn and Chereskin* [2009], the 6 hourly NCEP/CFSR reanalysis winds are used to obtain drift parameters. This is to keep MR measurements and filtered Stokes drift comparable, since the same NCEP/CFSR wind product was used to force WW3 (see section 3). Note that results would not change significantly if we used the ship anemometer winds instead. (A comparison between the shipboard and model winds, referenced to 10 m height, yields a correlation coefficient and mean directional difference length of 0.80 and 0.95 for wind speed and direction, respectively. The corresponding standard deviations are 1.98 m s^{-1} and 18.35°, with biases of -0.24 m s^{-1} and -6.0°.)

Covering all four cruises, Figure 11 shows time series of the 3 h averaged MR-ADCP differences and the NCEP/CFSR winds. The figure also includes a plot with the differences between the NCEP/CFSR wind direction and the shallowest MR current direction. With the exception of RR1015, during which the wind-current angles were relatively stable, a given angle rarely persists longer than a few hours (Figure 11, first plot). We need to keep this in mind when interpreting the results of our study, since there is likely to be a delay in the upper-ocean current response to changing wind stresses [e.g., *Muscarella et al*., 2011]. The second and third plots of Figure 11 illustrate the difference flow between the shallowest and deepest (2 and 8 m) MR measurements on

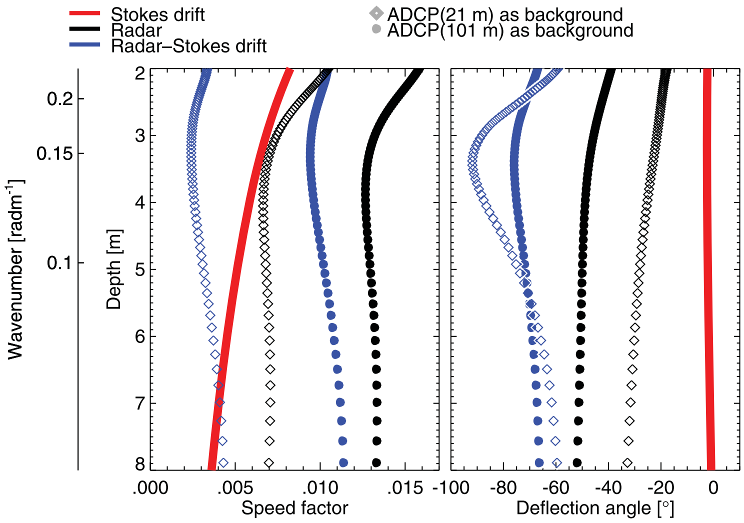

Figure 12. Near-surface drift parameters obtained from MR before (black) and after (blue) subtracting the filtered Stokes drift (red). For data shown as dots, the 101 m ADCP measurements were used as background current. Diamonds indicate that 21 m ADCP measurements were used. Results correspond to the average over all four cruises and are based on the 6 hourly NCEP/CFSR reanalysis winds. Negative directions indicate a CW deflection relative to the wind. The effective depth was computed assuming a linear profile.

the one hand and the shallowest (21 m) ADCP measurement on the other. The difference flow is relatively weak, but typically above the measurement noise level of both MR and ADCP. (In the previous subsection, Figure 10, we estimated the MR accuracy to be on the order of 1–3 cm s^{-1}. To estimate the ADCP accuracy, we compared measurements from the two ADCPs aboard the *Revelle*, NB150 and OS75. The agreement between current speeds and directions evaluated at 21 m is very good, with both correlation coefficient and mean directional difference length at 0.98, standard deviations of 0.04 m s^{-1} and 11.3°, and negligible biases. We therefore expect that MR and ADCP provide comparable accuracies.) It generally goes to the right of the wind, with the MR (2 m)-ADCP (21 m) flow more closely aligned with the wind than the MR (8 m)-ADCP (21 m) one. The former also tends to be greater in speed. These findings are in accordance with Ekman theory. Lastly, the fourth and fifth plots of Figure 11 show the difference speed and direction between the same (2 and 8 m) MR and the 101 m ADCP currents. The difference flow is stronger, but has much less coherence with the wind. It exhibits multiple CW around-the-compass rotations. (During RR1010, the third plot shows similar rotations.) These are due to inertial motions, which are essentially depth-independent inside the mixed layer, but have been shown to decrease by an order of magnitude directly below [*Weller*, 1982]. The MR-ADCP (101 m) difference flow is thus a function of the full wind history, and not just a function of the local instantaneous wind. However, *Ardhuin et al.* [2009] found that inertial motions do not significantly alter average Ekman flow results, although they do lead to an increased scatter. Here we make the common assumption that contributions due to inertial motions will average out [e.g., *Chereskin*, 1995].

Figure 12 shows the MR-based Ekman drift parameters over the depth range between 2 and 8 m. Results are shown for ADCP background currents measured at depths of 101 and 21 m. The drift parameters were determined by transforming the MR-ADCP difference flow profiles from a geographic to a wind-oriented coordinate frame. The resulting profiles were divided by their respective wind speeds, to obtain the speed factor, and then averaged. The figure also includes the WW3-based filtered Stokes drift (equation (2)), transformed in the same manner as the MR results. Lastly, it shows the quasi-Eulerian flow that results if the filtered Stokes drift is subtracted from the MR measurements.

The Ekman profile obtained from the MR-ADCP (101 m) difference flow exhibits the classic spiral structure, as originally predicted by *Ekman* [1905]. The deflection angle increases from 38.9° to the right of the wind at 2 m effective depth to 52.1° at 8 m, while the speed factor decreases from 1.58 to 1.32%. The rate at which the deflection angle increases can be seen to decrease with growing effective depth. The speed factor's decrease occurs down to an effective depth of ~4 m, at which point it remains approximately constant. In view of the difficulties that we face with this particular data set—it is relatively short, dominated by nonlocal processes, and has a constantly changing wind-current angle at the surface, allowing little time for an Ekman flow to establish, these results are in surprisingly good agreement with values reported in the literature [*Lewis and Belcher*, 2004].

The filtered Stokes drift decays exponentially with increasing effective depth. Speed factors range from 0.83 to 0.36%, and its direction is nearly constant windward (0.9° and 2.3° to the right of the wind at 2 and 8 m effective depth, respectively). Thus, the filtered Stokes drift has magnitudes that are ~50% of the wind and wave-drift at 2 m and ~25% at 8 m. The importance of the Stokes drift for near-surface flow is well established, with comparable values found by *Mao and Heron* [2008] and *Ardhuin et al*. [2009]. The MR-ADCP (21 m) Ekman drift parameters have similar depth dependencies as found for a 101 m background current, but magnitudes are smaller. Here the speed factor decreases from 1.05 to 0.70% and the deflection angle increases from 17.8° to 33.0° over 2 to 8 m effective depth. Lastly, the figure includes the quasi-Eulerian flow that results if we subtract the filtered Stokes drift from the MR-ADCP difference flow. This leads to decreased speed factors, increased deflection angles, and a reduced degree of variability with depth. For both background current depths, the deflection angle of the quasi-Eulerian flow peaks at effective depths between 3 and 4 m.

6. Conclusions and Outlook

A new technology to retrieve near-surface vertical current shear from MR image sequences was introduced. It exploits *Stewart and Joy*'s [1974] finding that radar-derived currents represent a weighted mean over the upper ocean flow. The current estimates' effective depth increases with the ocean wave length on which they are based. The standard MR current retrieval method pioneered by *Young et al*. [1985b] and *Senet et al*. [2001] yields a single current vector attributed to the "near surface." Although the method proposed here is closely related to theirs, several modifications had to be implemented to retrieve current shear. First, instead of retrieving currents from small analysis windows, we analyze the whole radar FOV. This requires a backscatter ramp correction that accounts for the radar return's dependency on range and azimuth, which we accomplished through a combination of temporal averaging and Fourier fitting. Second, we eliminated the "snapshot" simplification by trilinearly interpolating and georeferencing the raw polar radar data to a Cartesian grid. This addresses a number of shortcomings of the traditional ship-based coordinate frame. Most importantly, it makes our measurements insensitive to course changes. Third, we quantify and exploit the structure of the background noise within the 3-D power density spectra. This allows their conversion to SNR spectra, enhancing our ability to isolate the wave signal over a broad range of directions and frequencies. We employ *Senet et al*.'s [2001] iterative least squares regression algorithm to retrieve current vectors, but instead of treating all spectral coordinates attributed to the waves in bulk, we perform the analysis as a function of wave number. The result is an array of ~100 independent current estimates covering the upper ~10 m of the water column (assuming a linear profile).

The method's effectiveness was demonstrated using MR data collected from the *Revelle* during the ITOP 2010 field experiment in the western Pacific off Taiwan. The radar measurements were complemented by shipboard ADCP and anemometer data as well as WW3 modeling results. Our main findings can be summarized as follows: (1) The MR near-surface currents are in excellent agreement with the 21 m ADCP measurements, suggesting an accuracy that is comparable with more traditional current sensors. (2) The MR near-surface current profiles' response to wind and wave forcing is in accord with physical expectations. A great variety of near-surface flow behaviors was observed and explained, including several cases of flow reversal during a period that was characterized by unusually weak background currents. (3) The mean MR Ekman flow is in good agreement with previously reported values [*Lewis and Belcher*, 2004]. At an effective depth of 2 m, it is ~1.6% of the wind speed and ~38.9° to the right of the wind. With increasing effective depth, the speed factor is found to decrease and the deflection angle increase. After subtracting the filtered Stokes drift, which accounts for more than half of the wind drift at the shallowest depth, the resulting quasi-Eulerian current has an increased deflection angle and reduced variability in the vertical.

We are currently investigating the implications of our method for MR wave retrieval. Existing methods assume a vertically uniform near-surface flow [e.g., *Nieto Borge et al*., 2004]. We expect that MR wave spectra will become more reliable if near-surface current shear is accounted for. In the future, we hope to apply the technology developed here to data sets for which reference measurements of the near-surface vertical current shear are available. In addition, we plan to explore the extent to which the size of the analysis window can be reduced without compromising current shear results [cf. *Hessner et al*., 2014]. MR near-surface vertical current shear retrieval still has significant potential for improvement. For example, studies have shown that VV-polarized antennas yield better current results than the more standard HH antenna used here [e.g., *Huang and Gill*, 2012]. We hope that this paper will generate more interest in MR-based currents, and that they will ultimately improve our understanding of the physical processes occurring at the air-sea interface.

Acknowledgments
Funding for this work was provided by the U.S. Office of Naval Research under grants N00014-09-1-0392 and N00014-13-1-0288. B.L. acknowledges support as an International Research Fellow of the Japan Society for the Promotion of Science. We are grateful to E. Terrill, University of California, San Diego, for providing the marine X-band radar on R/V *Roger Revelle*. We also thank the captains, crews, and scientific parties of the *Revelle* ITOP cruises as well as the ASIS-EASI buoy team for their support in the field. Data can be made available for scientific purposes upon request to B.L. (blund@rsmas.miami.edu).

References

Alpers, W. R., D. B. Ross, and C. L. Rufenach (1981), On the detectability of ocean surface waves by real and synthetic aperture radar, *J. Geophys. Res.*, *86*(C7), 6481–6498.

Ardhuin, F., L. Marié, N. Rascle, P. Forget, and A. Roland (2009), Observation and estimation of Lagrangian, Stokes, and Eulerian currents induced by wind and waves at the sea surface, *J. Phys. Oceanogr.*, *39*(11), 2820–2838.

Barrick, D. E. (1968), A review of scattering from surfaces with different roughness scales, *Radio Sci.*, *3*, 865–868.

Barrick, D. E., M. W. Evans, and B. L. Weber (1977), Ocean surface currents mapped by radar, *Science*, *198*(4313), 138–144.

Beal, L. M., J. M. Hummon, E. Williams, O. B. Brown, W. Baringer, and E. J. Kearns (2008), Five years of Florida current structure and transport from the Royal Caribbean cruise ship Explorer of the Seas, *J. Geophys. Res.*, *113*, C06001, doi:10.1029/2007JC004154.

Beardsley, R. C., W. C. Boicourt, L. C. Huff, J. R. McCullough, and J. Scott (1981), CMICE: A near-surface current meter intercomparison experiment, *Deep Sea Res., Part I*, *28*(12), 1577–1603.

Bell, P. S., and J. C. Osler (2011), Mapping bathymetry using X-band marine radar data recorded from a moving vessel, *Ocean Dyn.*, *61*(12), 2141–2156, doi:10.1007/s10236-011-0478-4.

Broche, P., J. C. Demaistre, and P. Forget (1983), Mesure par radar décamétrique cohérent des courants superficiels engendrés par le vent, *Oceanol. Acta*, *6*(1), 43–53.

Campana, J., E. Terrill, and T. de Paolo (2015), Observations of surface current and current shear using X-band radar, in *IEEE/OES Eleventh Current, Waves and Turbulence Measurement (CWTM)*, pp. 1–5, IEEE, St. Petersburg, Fla.

Chereskin, T. K. (1995), Direct evidence for an Ekman balance in the California current, *J. Geophys. Res.*, *100*(C9), 18,261–18,269, doi:10.1029/95JC02182.

Chereskin, T. K., and D. Roemmich (1991), A comparison of measured and wind-derived Ekman transport at 11°N in the Atlantic Ocean, *J. Phys. Oceanogr.*, *21*(6), 869–878.

Collins, C. O., III, B. Lund, R. J. Ramos, W. M. Drennan, and H. C. Graber (2014), Wave measurement intercomparison and platform evaluation during the ITOP (2010) experiment, *J. Atmos. Oceanic Technol.*, *31*(10), 2309–2329.

D'Asaro, E., et al. (2014), Impact of typhoons on the ocean in the Pacific: ITOP, *Bull. Am. Meteorol. Soc.*, *95*(9), 1405–1418.

Davis, R., R. deSzoeke, D. Halpern, and P. Niiler (1981), Variability in the upper ocean during MILE. Part I: The heat and momentum balances, *Deep Sea Res., Part I*, *28*(12), 1427–1451.

Dean, R. G., and R. A. Dalrymple (1991), *Water Wave Mechanics for Engineers and Scientists*, World Scientific, Singapore.

Dittmer, J. (1995), Use of marine radars for real time wave field survey and speeding up transmission/processing, in *Proceedings of the WMO/IOC Workshop on Operational Ocean Monitoring Using Surface Based Radars*, vol. 32, pp. 133–137, WMO, Geneva, Switzerland.

Drennan, W. M., H. C. Graber, C. O. Collins III, A. Herrera, H. Potter, R. J. Ramos, and N. J. Williams (2014), EASI: An air-sea interaction buoy for high winds, *J. Atmos. Oceanic Technol.*, *31*(6), 1397–1409.

Ekman, V. W. (1905), On the influence of the Earth's rotation on ocean currents, *Ark. Mat. Astron. Fys.*, *2*, 1–53.

Fernandez, D. M., J. F. Vesecky, and C. C. Teague (1996), Measurements of upper ocean surface current shear with high-frequency radar, *J. Geophys. Res. C*, *101*(C12), 28,615–28,625, doi:10.1029/96JC03108.

Firing, E., and J. M. Hummon (2010), Shipboard ADCP measurements, The GO-SHIP repeat hydrography manual: A collection of expert reports and guidelines, *IOCCP Rep., ICPO*, 14, 1–11, Qingdao, China. [Available at http://www.go-ship.org/HydroMan.html.]

Firing, E., J. Hummon, and T. Chereskin (2012), Improving the quality and accessibility of current profile measurements in the Southern Ocean, *Oceanography*, *25*(3), 164–165.

Gommenginger, C. P., N. P. Ward, G. J. Fisher, I. S. Robinson, and S. R. Boxall (2000), Quantitative microwave backscatter measurements from the ocean surface using digital marine radar images, *J. Atmos. Oceanic Technol.*, *17*(5), 665–678, doi:10.1175/1520-0426(2000)017 < 0665:QMBMFT > 2.0.CO;2.

Graber, H. C., E. A. Terray, M. A. Donelan, W. M. Drennan, J. C. Van Leer, and D. B. Peters (2000), ASIS—A new air-sea interaction spar buoy: Design and performance at sea, *J. Atmos. Oceanic Technol.*, *17*(5), 708–720, doi:10.1175/1520-0426(2000)017 < 0708:AANASI > 2.0.CO;2.

Ha, E.-C. (1979), Remote sensing of ocean surface current and current shear by HF backscatter radar, technical report, DTIC Document D415-1, DTIC, Fort Belvoir, Va.

Hessner, K., K. Reichert, J. C. Nieto Borge, C. L. Stevens, and M. J. Smith (2014), High-resolution X-band radar measurements of currents, bathymetry and sea state in highly inhomogeneous coastal areas, *Ocean Dyn.*, *64*(7), NOAA Earth System Research Laboratory, Boulder, Colo. 989–998.

Hill, R. J. (2005), Motion compensation for shipborne radars and lidars, technical report, NOAA Technical Memorandum OAR PSD 309, NOAA Earth System Research Laboratory, Boulder, Colo.

Huang, W., and E. Gill (2012), Surface current measurement under low sea state using dual polarized X-band nautical radar, *IEEE J. Select. Top. Appl. Earth Obs.*, *5*(6), 1868–1873, doi:10.1109/JSTARS.2012.2208179.

IOC, IHO, and BODC (2003), *Centenary Edition of the GEBCO Digital Atlas [CD-ROM]*, Liverpool, U. K.

Jan, S., R.-C. Lien, and C.-H. Ting (2008), Numerical study of baroclinic tides in Luzon Strait, *J. Oceanogr.*, *64*(5), 789–802.

Kirby, J. T., and T.-M. Chen (1989), Surface waves on vertically sheared flows: Approximate dispersion relations, *J. Geophys. Res.*, *94*(C1), 1013–1027, doi:10.1029/JC094iC01p01013.

Lenn, Y.-D., and T. K. Chereskin (2009), Observations of Ekman currents in the Southern Ocean, *J. Phys. Oceanogr.*, *39*(3), 768–779.

Lewis, D., and S. Belcher (2004), Time-dependent, coupled, Ekman boundary layer solutions incorporating Stokes drift, *Dyn. Atmos. Oceans*, *37*(4), 313–351.

Lund, B., H. C. Graber, and R. Romeiser (2012), Wind retrieval from shipborne nautical X-band radar data, *IEEE Trans. Geosci. Remote Sens.*, *50*(10), 3800–3811, doi:10.1109/TGRS.2012.2186457.

Lund, B., C. O. Collins III, H. C. Graber, E. Terrill, and T. H. C. Herbers (2014), Marine radar ocean wave retrieval's dependency on range and azimuth, *Ocean Dyn.*, *64*(7), 999–1018.

Lund, B., H. C. Graber, J. Campana, and E. Terrill (2015a), Near-surface current shear measured by marine X-band radar, in *IEEE/OES Eleventh Current, Waves and Turbulence Measurement (CWTM)*, pp. 1–6, IEEE, St. Petersburg, Fla.

Lund, B., H. C. Graber, K. Hessner, and N. J. Williams (2015b), On shipboard marine X-band radar near-surface current "calibration", *J. Atmos. Oceanic Technol.*, *32*(10), 1928–1944, doi:10.1175/JTECH-D-14-00175.1.

Madsen, O. S. (1977), A realistic model of the wind-induced Ekman boundary layer, *J. Phys. Oceanogr.*, *7*(2), 248–255.

Mao, Y., and M. L. Heron (2008), The influence of fetch on the response of surface currents to wind studied by HF ocean surface radar, *J. Phys. Oceanogr.*, *38*(5), 1107–1121.

McWilliams, J. C., E. Huckle, J.-H. Liang, and P. P. Sullivan (2012), The wavy Ekman layer: Langmuir circulations, breaking waves, and Reynolds stress, *J. Phys. Oceanogr.*, *42*(11), 1793–1816.

Miyazawa, Y., R. Zhang, X. Guo, H. Tamura, D. Ambe, J.-S. Lee, A. Okuno, H. Yoshinari, T. Setou, and K. Komatsu (2009), Water mass variability in the western North Pacific detected in a 15-year eddy resolving ocean reanalysis, *J. Oceanogr.*, *65*(6), 737–756.

Muscarella, P. A., N. P. Barton, B. L. Lipphardt Jr., D. E. Veron, K. C. Wong, and A. D. Kirwan Jr. (2011), Surface currents and winds at the Delaware Bay mouth, *Cont. Shelf Res.*, *31*(12), 1282–1293.

Nieto Borge, J. C., and C. Guedes Soares (2000), Analysis of directional wave fields using X-band navigation radar, *Coastal Eng.*, *40*(4), 375–391.

Nieto Borge, J. C., G. R. Rodríguez, K. Hessner, and P. I. González (2004), Inversion of marine radar images for surface wave analysis, *J. Atmos. Oceanic Technol.*, *21*(8), 1291–1300.

Plant, W. J. (2003), Microwave sea return at moderate to high incidence angles, *Waves Random Media*, *13*(4), 339–354.

Polton, J. A., D. M. Lewis, and S. E. Belcher (2005), The role of wave-induced Coriolis-Stokes forcing on the wind-driven mixed layer, *J. Phys. Oceanogr.*, *35*(4), 444–457.

Price, J. F., R. A. Weller, and R. R. Schudlich (1987), Wind-driven ocean currents and Ekman transport, *Science*, *238*, 1534–1538.

Ralph, E. A., and P. P. Niiler (1999), Wind-driven currents in the tropical Pacific, *J. Phys. Oceanogr.*, *29*(9), 2121–2129.

Richman, J. G., R. A. de Szoeke, and R. E. Davis (1987), Measurements of near-surface shear in the ocean, *J. Geophys. Res.*, *92*(C3), 2851–2858, doi:10.1029/JC092iC03p02851.

Rogers, W. E., and D. W. C. Wang (2007), Directional validation of wave predictions, *J. Atmos. Oceanic Technol.*, *24*(3), 504–520.

Saha, S., et al. (2010), The NCEP climate forecast system reanalysis, *Bull. Am. Meteorol. Soc.*, *91*(8), 1015–1057.

Schudlich, R. R., and J. F. Price (1998), Observations of seasonal variation in the Ekman layer, *J. Phys. Oceanogr.*, *28*(6), 1187–1204.

Seemann, J., F. Ziemer, and C. M. Senet (1997), A method for computing calibrated ocean wave spectra from measurements with a nautical X-band radar, in *MTS/IEEE Conference Proceedings on OCEANS'97*, vol. 2, pp. 1148–1154, IEEE, Halifax, NS, doi:10.1109/OCEANS.1997.624154.

Senet, C. M., J. Seemann, and F. Ziemer (2001), The near-surface current velocity determined from image sequences of the sea surface, *IEEE Trans. Geosci. Remote Sens.*, *39*(3), 492–505.

Shen, C., W. Huang, E. W. Gill, R. Carrasco, and J. Horstmann (2015), An algorithm for surface current retrieval from X-band marine radar images, *Remote Sens.*, *7*(6), 7753–7767, doi:10.3390/rs70607753.

Smith, M. J., E. M. Poulter, and J. A. McGregor (1996), Doppler radar measurements of wave groups and breaking waves, *J. Geophys. Res.*, *101*(C6), 14,269–14,282, doi:10.1029/96JC00766.

Smith, S. D. (1980), Wind stress and heat flux over the ocean in gale force winds, *J. Geophys. Res.*, *10*(5), 709–726.

Stevens, C. L., E. M. Poulter, M. J. Smith, and J. A. McGregor (1999), Nonlinear features in wave-resolving microwave radar observations of ocean waves, *IEEE J. Oceanic Eng.*, *24*(4), 470–480.

Stewart, R. H., and J. W. Joy (1974), HF radio measurements of surface currents, *Deep Sea Res. Oceanogr. Abstr.*, *21*(12), 1039–1049.

Sullivan, P. P., J. C. McWilliams, and W. K. Melville (2007), Surface gravity wave effects in the oceanic boundary layer: Large-eddy simulation with vortex force and stochastic breakers, *J. Fluid Mech.*, *593*, 405–452, doi:10.1017/S002211200700897X.

Tamura, H., Y. Miyazawa, and L.-Y. Oey (2012), The Stokes drift and wave induced-mass flux in the north Pacific, *J. Geophys. Res.*, *117*, C08021, doi:10.1029/2012JC008113.

Teague, C. C., J. F. Vesecky, and Z. R. Hallock (2001), A comparison of multifrequency HF radar and ADCP measurements of near-surface currents during COPE-3, *IEEE J. Oceanic Eng.*, *26*(3), 399–405.

Tolman, H. L. (2009), *User Manual and System Documentation of WAVEWATCH III Version 3.14, Technical Note, MMAB Contrib*, NCEP, Camp Springs, Md. 276, NCEP, Camp Springs, Md.

Trizna, D. B., J. P. Hansen, P. Hwang, and J. Wu (1991), Laboratory studies of radar sea spikes at low grazing angles, *J. Geophys. Res.*, *96*(C7), 12,529–12,537.

Ullman, D. S., J. O'Donnell, J. Kohut, T. Fake, and A. Allen (2006), Trajectory prediction using HF radar surface currents: Monte Carlo simulations of prediction uncertainties, *J. Geophys. Res.*, *111*, C12005, doi:10.1029/2006JC003715.

Varlamov, S. M., X. Guo, T. Miyama, K. Ichikawa, T. Waseda, and Y. Miyazawa (2015), M2 baroclinic tide variability modulated by the ocean circulation south of Japan, *J. Geophys. Res. Oceans*, *120*, 3681–3710, doi:10.1002/2015JC010739.

Weber, B. L., and D. E. Barrick (1977), On the nonlinear theory for gravity waves on the ocean's surface. Part I: Derivations, *J. Phys. Oceanogr.*, *7*(1), 3–10.

Weller, R. A. (1982), The relation of near-inertial motions observed in the mixed layer during the JASIN (1978) experiment to the local wind stress and to the quasi-geostrophic flow field, *J. Phys. Oceanogr.*, *12*(10), 1122–1136.

Wetzel, L. B. (1990), Surface waves and fluxes, in *Electromagnetic Scattering From the Sea at Low Grazing Angles*, pp. 109–171, Kluwer, Dordrecht, Netherlands.

Wright, J. (1968), A new model for sea clutter, *IEEE Trans. Antennas Propag.*, *16*(2), 217–223.

Yoshikawa, Y., and A. Masuda (2009), Seasonal variations in the speed factor and deflection angle of the wind-driven surface flow in the Tsushima Strait, *J. Geophys. Res.*, *114*, C12022, doi:10.1029/2009JC005632.

Yoshikawa, Y., T. Matsuno, K. Marubayashi, and K. Fukudome (2007), A surface velocity spiral observed with ADCP and HF radar in the Tsushima Strait, *J. Geophys. Res.*, *112*, C06022, doi:10.1029/2006JC003625.

Young, I. R., W. Rosenthal, and F. Ziemer (1985a), Marine radar measurements of waves and currents during turning winds, *Ocean Dyn.*, *38*, 23–38, doi:10.1007/BF02226434.

Young, I. R., W. Rosenthal, and F. Ziemer (1985b), A three-dimensional analysis of marine radar images for the determination of ocean wave directionality and surface currents, *J. Geophys. Res.*, *90*(C1), 1049–1059.

Ziemer, F. (1995), An instrument for the survey of the directionality of the ocean wave field, in *Proceedings of the WMO/IOC Workshop on Operational Ocean Monitoring Using Surface Based Radars*, vol. 32, pp. 81–87, WMO, Geneva, Switzerland.